SPARC-BD-03/001
8 April 2003

STATUS OF THE BEAM DYNAMICS STUDIES FOR THE SPARC PROJECT

D. Alesini, M. E. Biagini, M. Boscolo, M. Ferrario, V. Fusco, S. Guiducci, M. Migliorati, L. Palumbo, B. Spataro, C. Vaccarezza, *(INFN/LNF),* A. Bacci, L. Serafini, *(INFN /Milano),* R. Bartolini, L. Giannessi, L. Mezi, L. Picardi, M. Quattromini, C. Ronsivalle *(ENEA/FIS),* J. Rosenzweig *(UCLA)*

Abstract

We report in this paper the results of the beam dynamics group activities in the last year in preparation of the preliminary SPARC Technical Design Report.

Extended version of SPARC Preliminary TDR Ch. 3

1 INTRODUCTION

We report in this paper the results of the beam dynamics group activities in the last year in preparation of the preliminary SPARC Technical Design Report.

2 SPARC LAYOUT

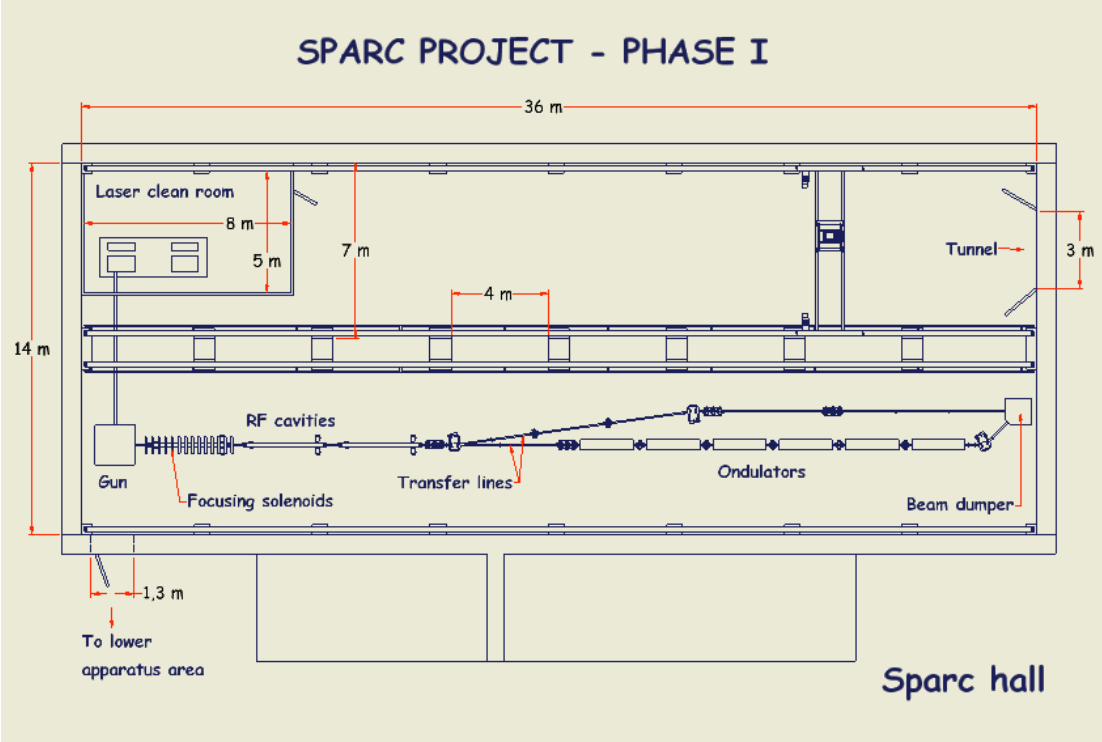

Figure 2.1: *Schematic of layout of the SPARC photo-injector complex inside the SPARC experimental hall, including undulator, and by-pass line (Phase 1).*

The proposed system to be built consists of: a 1.6 cell RF gun operated at S-band (2.856 GHz, of the BNL/UCLA/SLAC type) and high peak field on the cathode (≥120 MV/m) with incorporated metallic photo-cathode (Copper or Mg), generating a ≥5.6 MeV beam which is properly focused and matched into 3 accelerating sections of the SLAC type (S-band, travelling wave) which accelerate the bunch up to 150-200 MeV. The final layout of SPARC showing Phase 1 is displayed in Fig. 2.1.

The production of highest brightness electron beams in the photo-injector requires that a temporally-flat, picosecond laser source be used to drive the photo-cathode. The laser system driving the photocathode will therefore employ high bandwidth Ti:Sa technologies with the oscillator pulse train locked to the RF (Fig. 2.2). The Ti:Sa mode locked oscillator and amplifiers able to produce the requested energy per pulse (500 μJ at 266 nm) are commercially available. To obtain the desired time pulse shape we will test the manipulation of frequency lines in the large bandwidth of Ti:Sa, in order to produce the 10 ps long flat-top shape. We plan to

use a liquid crystal mask in the Fourier plane of the non-dispersive optic arrangement or a collinear acousto-optic modulator for linear frequency manipulation.

The SASE FEL experiment will be conducted using a permanent magnet undulator made of 6 sections, each 2.13 m long, separated by 0.36 m gaps, and featuring single quadrupoles which focus the electron beam in the horizontal plane. The undulator period is set at 3.0 cm, with an undulator parameter k_w = 1.4.

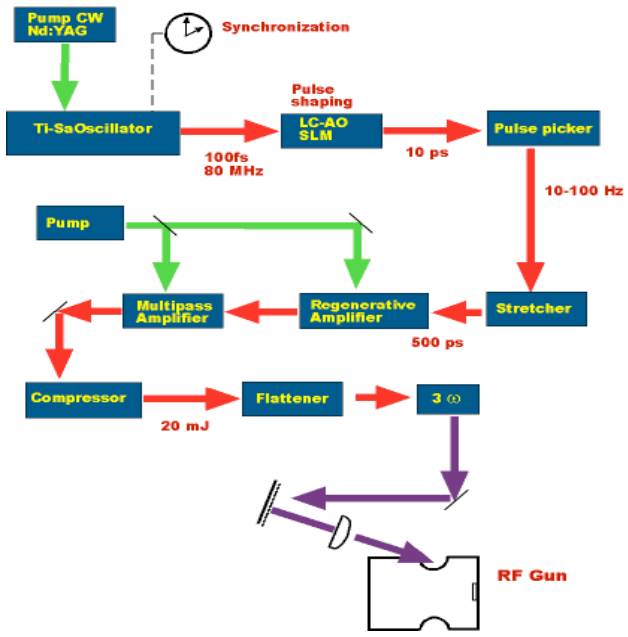

Figure 2.2: *Layout of the photocathode laser system.*

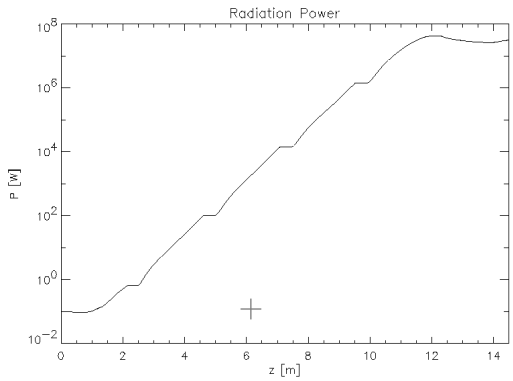

Figure 2.3: *Radiation Power at 530 nm growth along the undulator, from GENESIS simulation.*

A simulation performed with GENESIS is reported in Fig.2.3, showing the exponential growth of the radiation power at 530 nm along the undulator; almost 10^8 W can be reached after 14 m of total undulator length. Preliminary evaluations of the radiation power generated into the non-linear coherent odd higher harmonics show that 10^7 and $7x10^5$ W can be reached on the third and fifth harmonics, respectively.

The second beam line is envisioned to by-pass the undulator, thus experiments on magnetic pulse compression to be performed. In particular, in Phase 2, it is foreseen to investigate emittance degradation due to CSR induced effects on and surface roughness wake-field effects.

3 PHOTO-INJECTOR DESIGN OPTIMIZATION

3.1 Overview

The SPARC photoinjector serves two requirements. First, it serves as test-bend for development of techniques and concepts in high brightness beam generation and manipulations. Second, and not less importantly, it is to be employed for driving a SASE FEL experiment at 530 nm, as discussed in the general project overview. The FEL requirements, being a test of the entire integrated system robustness at SPARC, may be taken, therefore, as the nominal design parameters for the injector. To meet the FEL requirements a high brightness (high current low emittance, $B_n = 2I/\varepsilon_n^2$) electron beam has to be generated, accelerated up to 155 MeV and transported up to the entrance of the undulator, minimizing the emittance and energy spread degradation due to correlated space charge and wake field effects.

In order to saturate the FEL radiation in the planned 15 m long undulator, and to additionally allow generation of higher harmonics, the design beam parameters are very rigorous: normalized emittance $\varepsilon_n < 1$ μm, relative energy spread $\Delta\gamma/\gamma < 0.1$ % and peak current $I \sim 90$ A. Fortunately, such parameters have to be reached only on the scale of the FEL cooperation length, which in our case is about 300 μm. With these demands in mind, detailed beam dynamics studies that allow current and phase space optimization have been performed. These include start-to-end simulations for the ideal case, in which all known realistic phenomena that affect the beam dynamics are included. These simulations display the sometimes subtle effects that details of the beam distribution in phase space on may exert on beam optimization and on FEL performance. This sensitivity has been noted in previous SASE FEL experiments using similar systems. Because of this need to know phase space details whenever possible, and to benchmark simulations so the other more difficult to measure parameters may be determined, simulation models have been developed for “virtual diagnostic experiments”. These simulations allow us to examine collective effects in measurements, and also give us fundamental insights about what one may actually measure, and learn about the beam dynamics systems, during the injector commissioning.

We discuss in this paper the present status of beam dynamics simulation activities. We begin in the following section by describing the simulation tools we have adopted or developed to study the beam dynamics of the SPARC project. The approach to achieving the design criteria and the start-to-end simulation for the nominal working point of the injector/FEL system are then discussed in Section 3.3. Phase 1a of the SPARC project will consist in the commissioning of the laser/rf photocathode gun/solenoid system (5.6 MeV beam), with a systematic measurement of the emittance compensation process along the subsequent drift. The main goal of this experiment is to collect as much information as possible about the 6D beam phase space

evolution, in order to obtain the capability of understanding and optimizing the SPARC system with full energy beam. A dedicated emittance-meter tool has been foreseen in this phase, as discussed in the diagnostic section of this TDR. This task is critical for benchmarking simulation tools, and can only be accomplished in Phase 1a, when there is no interference from post-acceleration linac hardware, In support of this delicate phase of the project, we have developed a simulation tool able to reproduce as closely as possible the proposed measurement technique, as discussed in Section 3.4. Similarly for phase 1b (155 MeV operation) we discuss the slice emittance measurement through examination of simulations. The effects of beam perturbations on the injector performance are studied Section 3.5.

Phase 2 of the project will consist mainly in beam compression techniques studies, via a magnetic chicane device and via a new technique based on the so-called velocity bunching. In Section 3.6 we discuss the injector performances comparing the two beam compression option foreseen, in particular the velocity bunching technique and its possible integration in a higher energy linac.

3.2 Simulation tools

It has been well established in the high brightness beam community that a start to end simulation of a SASE FEL experiment must be performed by means of the PARMELA-ELEGANT-GENESIS chain of codes [1]. We have adopted the same tools in our studies, and have additionally employed simpler codes that we have developed to speed up the process of beam parameter scanning, and more complex codes to study in more detail 3D effects. We cross-check the results across levels of complexity in this hierarchy of codes. We list below our arsenal of simulation codes, with short descriptions of their capabilities and range of applicability:

3.2.1 Simulation codes for the injector/linac:

— **PARMELA** is an electron-linac particle-dynamics code[2],[3]. It is a wide spread reliable multi-particle code that transforms the beam, represented by a collection of particles, through a user-specified linac and/or transport system, where field maps of magnets and accelerator cavities are derived from **POISSON** and **SUPERFISH**. It includes a 2-D and 3-D space-charge calculation in the “quasi static” approximation, and therefore does not include radiative effects in bends. Both LANL and UCLA versions of this code are employed in SPARC studies.

— **HOMDYN** relies on a multi-envelope model based on the time dependent evolution of a uniform bunch approximation[4]. The algorithm is very efficient and despite some strong simplifying assumptions it allows the quick relaxation of the large number of parameters involved in parameter studies, to quickly find a reasonably optimized configuration. After fast scanning with HOMDYN, PARMELA is typically used to explore the proposed working point. It does not presently have a strong model for bending systems

— **TREDI** provides a rigorous space charge fields description by taking into account the effects due to the finite propagation velocity of signals through the bunch with a 6D time dependent representation of beam dynamics[5]. Space charge forces are calculated by a Lienard-Wiechert retarded potential formalism. This is accomplished in TREDI by storing the histories of macro-particles trajectories, and by tracking back in time the source coordinates until the retarded condition is satisfied, a very memory-intensive process. The effects of boundaries for flat walls are included by the image charge method.

— **ABCI** computes wakes field, impedances and loss factors, by solving the Maxwell equation in the time domain for a Gaussian bunched beam propagating through an axi-symmetric structure on or off axis[6].

3.2.2 Simulation codes for beam transport

— **ELEGANT:** is an beam dynamics code that computes Twiss parameters, transport matrices, nonlinear transport to 3rd order, closed orbits, beam transport floor coordinates, error amplification factors, dynamic apertures, and more[7]. It performs 6-D tracking with matrices and/or canonical integrators, and supports a variety of time-dependent elements. It computes coherent synchrotron radiation effects using a 1D model, and also performs optimization algorithms *(e.g.,* matching), including optimization of tracking results.

— **MAD:** is a tool for charged-particles optics in alternating gradient accelerators and beam lines[8]. Includes linear lattice parameter calculation, linear lattice matching, transfer matrix matching, and particle tracking.

— **RETAR:** a 3D EM PIC code based on retarded potentials via an integral algorithm. It was recently developed by the SPARC group and is presently under test. It can describe in a self-consistent fashion the interaction of an electron bunch with its own self-field (velocity and radiation field). Only flat boundaries can be treated in the present version.

3.2.3 Simulation codes for free electron laser dynamics

— **GENESIS:** is a time-dependent three-dimensional FEL simulation code [9]. It is mainly devoted to the simulation of single pass free electron lasers, integrates the averaged electron motion in the undulator as it is coupled to the radiation fields, which evolve in the "slowly varying envelope approximation".

— **GINGER:** direct descendant of the LLNL FEL simulation code "FRED", GINGER as GENESIS is a KMR wiggler period averaged FEL code. The fields are assumed in cylindrical symmetry while the electron trajectories are integrated in 3D [10].

— **MEDUSA:** is a 3D, multifrequency, macroparticle simulation code that represents the electromagnetic field as a superposition of Gauss-Hermite modes and uses a source-dependent expansion to determine the evolution of the optical mode radius[11]. The field equations are integrated simultaneously with the Lorentz force equations. MEDUSA differs from other nonlinear simulation codes in that no undulator-period averaging is imposed on the electron dynamics.

— **PERSEO:** the "Perseo" FEL-cad library allows the 1D time dependent simulation of SASE FEL configurations, oscillator configurations and exotic configurations like MOPA, it includes higher order harmonics and startup from shot-noise[12].

— **PROMETEO:** is a 1D, multiparticle code based on a modified version of the Prosnitz, Szoke, and Neil formulation of FEL dynamical equations. The original model has been generalized to include the effect of beam emittance and the undulator errors. The code is capable of accounting for the evolution of the coherent generation of higher-order harmonics in SASE or oscillator FELs, including the optical klystron and segmented undulators [13].

3.3 Design criteria

A detailed theoretical study of the emittance compensation process in a photoinjector [14] has demonstrated that the optimization of a photoinjector corresponds to accelerating and propagating the beam through the device as closely as possible to two relevant beam equilibria: a laminar Brillouin flow in drifts and the so-called invariant envelope in accelerating sections, which is a generalization of Brillouin flow for an accelerated beam. In this case the beam undergoes cold plasma oscillations of spatial wavenumber k_p, in which the space charge collective force is largely dominant over the emittance pressure. The frequency of the plasma oscillations, due to mismatches between the space charge force and the external focusing gradient, is to first order independent of the current while the betatron motion (trajectory cross-over) is almost absent (laminar flow). In fact it is the frequency independence that leads to reversible normalised emittance oscillations: accelerating the beam on the invariant envelope damps these oscillations like the square root of the beam energy, so that the normalised emittance at the injector exit reduces to a steady state minimum when the oscillations are properly tuned.

It has been shown that the rms projected normalized transverse emittance $\varepsilon_n = \sqrt{\langle x^2 \rangle \langle (\gamma x')^2 \rangle - \langle x \gamma x' \rangle^2}$ oscillates with a frequency $\sqrt{2K_r} = k_p$ at an amplitude $\Delta\varepsilon_n \approx \sqrt{\hat{I}/I_0}$ whenever a bunched beam is rms matched into a focusing channel of gradient K_r, *i.e.* on a Brillouin flow equilibrium:

$$\sigma_B(\zeta) = \sqrt{\frac{\hat{I}(\zeta)}{2 I_0 \beta^3 K_r}} \tag{3.1}$$

where σ is the rms beam spot size, eventually slice dependent, $\zeta \equiv z - \beta ct + z_0$ is the slice position, $\hat{I}$ is the peak current and I_0=17 kA the Alfven current. In a similar way, accelerating on the invariant envelope,

$$\varepsilon_{inv}(z) = \frac{2}{\gamma\sqrt{\gamma}}\sqrt{\frac{\hat{I}(z)}{I_0}}, \tag{3.2}$$

where $\gamma = eE_{acc}/m_e c^2$ (E_{acc} is the accelerating field), which is a particular exact solution of the rms envelope equation in the laminar flow regime, leads to *damped* oscillations of the emittance, and secular diminishing of the amplitude of the oscillations.

The basic point in the design of a photoinjector is therefore to match properly the beam at injection into any accelerating section, according to these criteria:

$$\Gamma' = 0 \tag{3.3}$$

implying a laminar waist at injection and

$$\sigma = \frac{2}{k_w}\sqrt{\frac{\hat{I}}{2I_0\gamma}} \tag{3.4}$$

giving an rms match on the invariant envelope for a TW accelerating field.

The laminar regime extends up to an energy given by:

$$\gamma = \sqrt{\frac{8}{3}}\frac{\hat{I}}{2I_0\varepsilon_{th}\gamma} \tag{3.5}$$

where ε_{th} is the thermal emittance. With the expected SPARC parameters: $\hat{I}$=90 A, E_{acc}=25 MV/m and an estimated [15] thermal emittance of 0.3 μm for a Cu cathode with UV excitation, the transition occurs around 150 MeV (this estimate assumes little additional uncorrelated emittance is added through nonlinear space-charge forces and other effects[16]). For this reason the emittance compensation process of the SPARC injector has to be optimized up to the exit of the booster linac, before injecting the beam in the undulator through the transfer line, which in turn must be examined for its emittance preserving properties.

Following the previous matching condition a new working point very suitable to damp emittance oscillations has been recently found [17] in the context of the LCLS FEL project [18] and adopted also by the TESLA-FEL[19] and ORION[20] facilities. By a proper choice of rf gun and solenoid parameters, the emittance evolution shows a double minimum behavior in the drifting region (see simulations in Chapter 4), caused by a chromatic effect occurring in the solenoid[21]. If the booster is located where the relative emittance maximum and the envelope waist occur, the second emittance minimum can be shifted at the booster exit line as shown in following figure and frozen at a very low level, preventing additional emittance oscillations in the subsequent beam propagation.

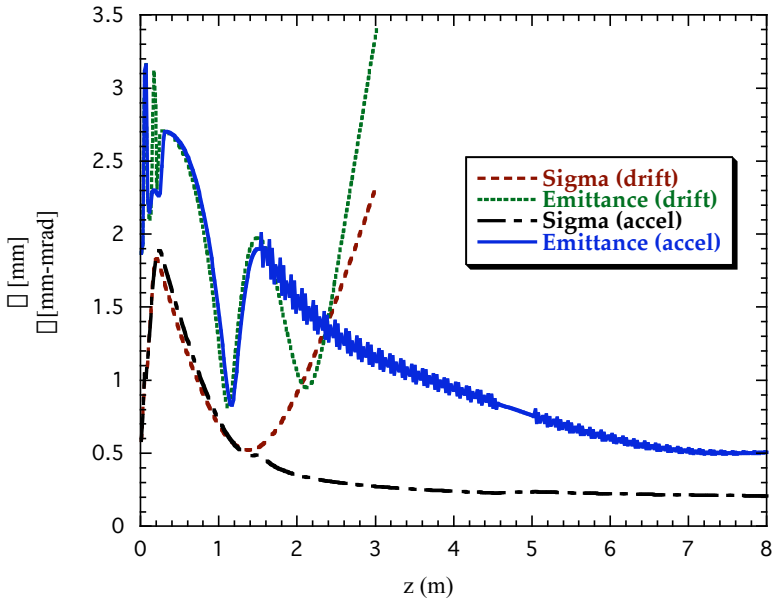

Figure 3.1. *HOMDYN simulation of SPARC injector transverse rms beam size and normalized emittance, in two TW linac configuration. Thermal emittance of 0.3 mm-mrad is assumed; additional focusing is provided around the first linac.*

Appendix A: Chromatic origin of the double emittance minimum

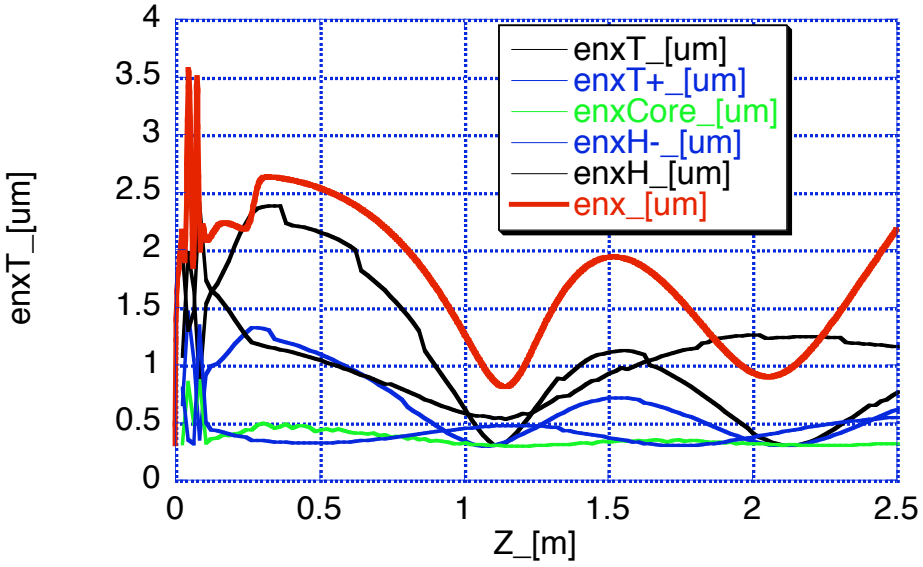

FIG. A1: Total rms normalized emittance for an S-band gun with solenoid (red bold line) from the cathode along a 2.3 m long drift, together with the rms normalized emittance computed for five representative 400 □m long slices, located at the longitudinal extrema and in the core of the bunch.

A slice analysis shows that the core of the bunch exhibits only minor emittances oscillation (it has very little effective variation of the defocusing space charge force) while the

tails experience a a noticeble oscillation driving also the total emittance oscillation see Fig. A1 and Fig. A2. The emittance compensation occuring in the booster when the invariant envelope matching conditions are satisfied is actually limited by the head and tail slice behavior; these slices also carry the most pronounced energy deviation, as shown in Fig. A3.

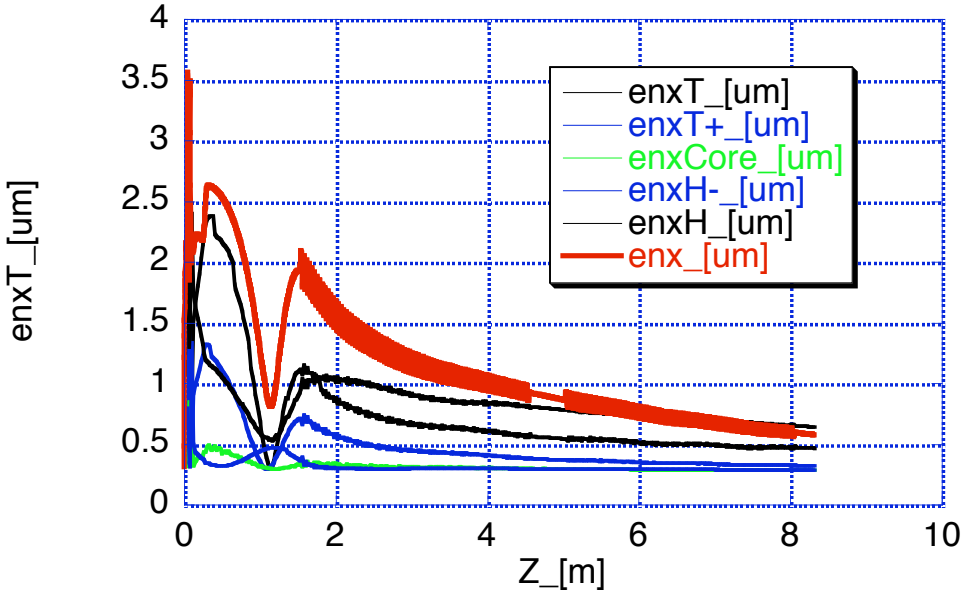

FIG. A2: Same as Fig. A1 but with a booster located at z=1.5 m.

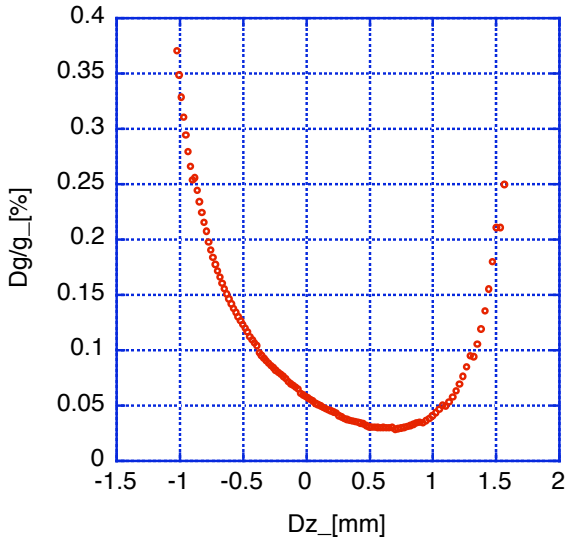

FIG. A3: Energy deviation along the bunch at z=0.2 (solenoid centre) computed for a 400 □m long slice centered at Dz.

The origin of the double emittance minimum downstream of the solenoid location can be explained as mainly due to a chromatic effect occuring inside the solenoid. Following [14], a simple heuristic example helps to understand this process. Let consider a beam traveling in a long solenoid channel without acceleration, subject to its own space charge field and an external focusing force. Such a beam can be described by the following rms envelope equation, neglecting the thermal emittance term:

$$\sigma'' + k^2\sigma = \frac{Ig(\zeta)}{2I_A\sigma^3} \tag{A.1}$$

where $k = \dfrac{eB}{2mc\gamma}$ is the external solenoid parameter (depending on γ), ζ is the coordinate along the bunch and $g(\zeta)$ is the space charge field form factor, that for a uniform charged cylinder with radius *R* and length *L* is given by [17]

$$g(\zeta) = \frac{1-\zeta/L}{2\sqrt{(1-\zeta/L)^2 + A^2}} + \frac{\zeta/L}{2\sqrt{(\zeta/L)^2 + A^2}}, \tag{A.2}$$

where $A = \dfrac{R}{\gamma L}$ is the bunch aspect ratio.

An equilibrium solution of Eq. A.1 can be easily found by setting $\sigma'' = 0$, leading to the already quoted Brillouin flow solution,

$$\sigma_{eq}(\gamma,\zeta) = \sqrt{\frac{Ig(\zeta)}{2I_A\gamma^3}}\,\frac{1}{k}. \tag{A.3}$$

Notice that each slice along the bunch, identified by its coordinate ζ, has a different equilibrium solution, not only because of the ζ dependence of the space charge field form factor, that from now on we will assume constant $g(\zeta) = 1$, but also because of the γ dependence of the solution. In case of a significant correlated energy spread along a cylindrical uniformly charged bunch with transverse size σ_c (assuming at the beginning each slice has the same σ_c) only the slice with the correct γ_0, if any, will be in equilibrium with a given external field *B*. Any other slice will oscillate around the initial size σ_c according to the solution of the linearized envelope equation about its equilibrium solution (assuming $\sigma' = 0$),

$$\sigma(z,\gamma,\zeta) = \sigma_{eq}(\gamma,\zeta) + \Delta\sigma(\gamma,\zeta)\cos\left(\sqrt{2}k(\zeta)z\right) \quad , \tag{A.4}$$

where $\Delta\sigma(\gamma,\zeta) = \sigma_c - \sigma_{eq}(\gamma,\zeta)$, as shown in Fig. A4.

Notice that in this case each slices has its own oscillation amplitude and its own oscillation frequency.

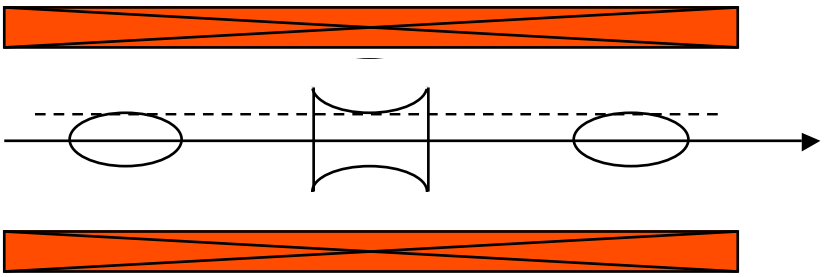

FIG. A4: Schematic representation of a Brillouin flow. Notice that only the central slice is in equilibrium, the other slices are oscillating around theyr own equilibrium solution.

Let us compute now the emittance oscillations of a bunch with a linear energy spread correlation entering in a long solenoid at a waist. Taking into account only two representative slices with a slightly different energy: $\gamma_+ = \gamma_o(1+\delta)$ and $\gamma_- = \gamma_o(1-\delta)$, where $\delta = \frac{\sigma_\gamma}{\gamma_o}$, the rms normalized emittance for a two slice bunch is given by

$$\varepsilon_n = \frac{\gamma}{2}\left|\sigma_+\sigma_{p-} - \sigma_{-p}\sigma_+\right|. \tag{A.5}$$

Substituting

$$\begin{aligned} \sigma_+ &= \sigma_{eq+} + \Delta\sigma_+ \cos\left(\sqrt{2}k_+ z\right) \\ \sigma_{p+} &= -\sqrt{2}k_+\Delta\sigma_+ \sin\left(\sqrt{2}k_+ z\right) \end{aligned} \quad \text{and} \quad \begin{aligned} \sigma_- &= \sigma_{eq-} + \Delta\sigma_- \cos\left(\sqrt{2}k_- z\right) \\ \sigma_{p-} &= -\sqrt{2}k_-\Delta\sigma_- \sin\left(\sqrt{2}k_- z\right) \end{aligned} \tag{A.6}$$

into to (A.5) one obtains, to first order in δ,

$$\varepsilon_n = \frac{\gamma}{\sqrt{2}}k_o\left|\sigma_{eqo}\left(2\Delta\sigma_o + \sigma_\delta\right)\sin\left(\frac{\Delta k}{2}z\right)\cos\left(\langle k\rangle z\right) + \Delta\sigma_o^2\sin\left(\Delta k z\right)\right| \tag{A.7}$$

where $\langle k\rangle = \frac{1}{\sqrt{2}}\left(k_+ + k_-\right) = \sqrt{2}k_o$ is the average beam plasma frequency, $\Delta k = \sqrt{2}\left(k_- - k_+\right) = 2\sqrt{2}k_o\delta$ the modulating plasma frequency and $\Delta\sigma_o = \sigma_c - \sigma_{eqo}$ is the envelope offset with respect to the nominal energy equilibrium solution. When $z << \frac{\pi}{2\Delta k}$ Eq. A.7 can be approximated by the following expression,

$$\varepsilon_n = \frac{\gamma}{\sqrt{2}}k_o\Delta\sigma_o\left|\left(\sigma_{eqo}\left(2\Delta\sigma_o + \sigma_\delta\right)\cos\left(\langle k\rangle z\right) + \Delta\sigma_o\right)\Delta k z\right|. \tag{A.8}$$

In Fig. A5, the average envelope and emittance oscillations predicted by Eq. A.7 are reported, and these qualitatively reproduce the double emittance minimum behavior around seen in the more complex photoinjector case discussed above.

When the initial envelope offset is not too far from the equilibrium solution (Eq. A.3), the

emittance oscillates with the average plasma frequency and periodically goes back to its initial value. By increasing the initial envelope offset the emittance evolution is dominated by the beating term and the original minimum is recovered only after a longer period, as shown in Fig. A6. This is a warning for beam operation in long solenoid devices in which the beam current varies as in the case of velocity bunching.

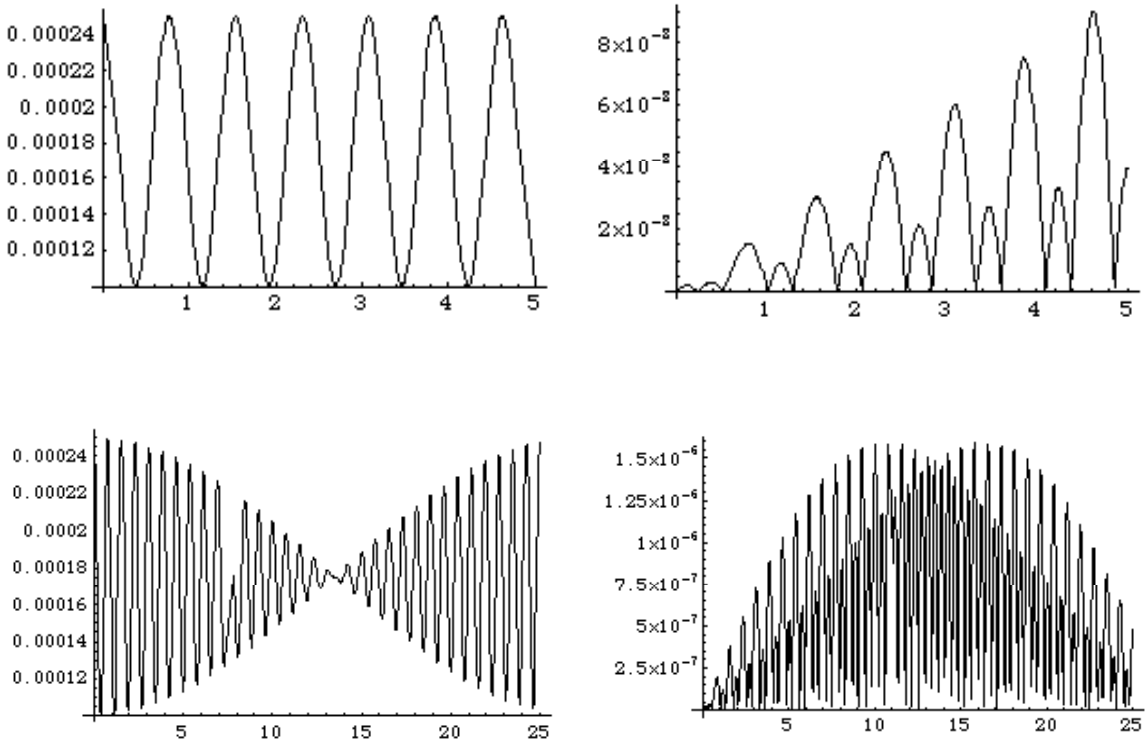

FIG. A5: Envelope (left) and normalized emittance (right) evolution, as predicted by Eq. A.7, reproducing the behavior of Fig. A1. Lower plots show a longer propagation length scales

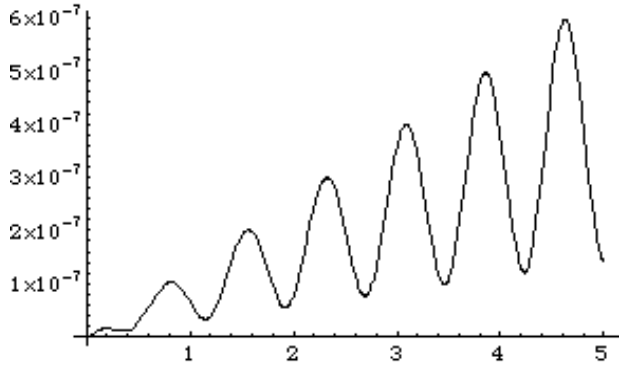

FIG. A6: Normalized emittance as predicted by Eq. A.7 with $\beta_c=3\beta_{eq0}$

This working point has been easily scaled to different gun RF frequency and bunch charge design through well-known techniques. It might also be convenient to operate the injector at a different gradient with respect to the original design, while keeping the beam line unchanged. In this case the scaling has to preserve the main feature of the original bunch in terms of average and beating plasma frequencies. A reduced gun peak field results in a lower energy gain, hence a

first scaling law can be deduced by the condition of keeping the average plasma frequency invariant,

$$B \quad \langle \rangle . \tag{A.9}$$

The beating plasma frequency is related to the relative energy spread along the bunch. The longitudinal phase space in the center of the solenoid (z=0.2 m) is shown in Fig. A7.

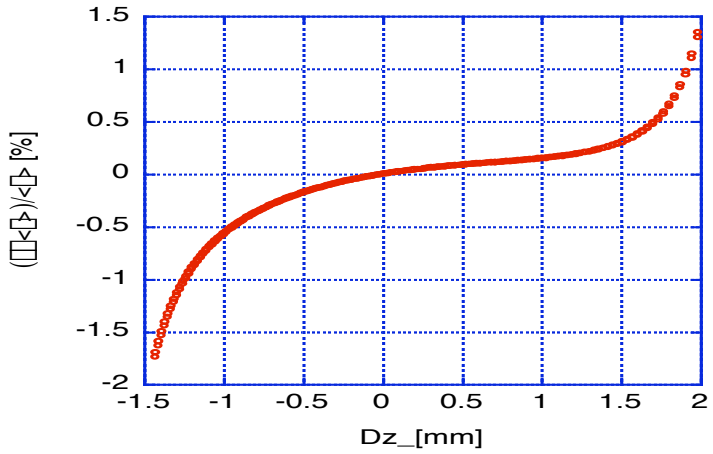

FIG. A7: Longitudinal phase space in the center of the solenoid (z=0.2 m)

As one may easily note the energy correlation is dominated by a third order longitudinal correlation typical of the longitudinal space charge-induced energy spread. To keep such a correlation one has to keep unchanged the beam aspect ratio A, resulting in

$$\frac{}{} \quad \langle \rangle , \tag{A.10}$$

and the current density $J \quad Q/ \; ^2_r$ scales like [39]

$$J \quad \langle \rangle^3 . \tag{A.11}$$

For a constant charge scaling, Eqs. A.10 and A.11 taken together imply that $\quad \langle \rangle^{-5/3}$ and $\quad \langle \rangle^{-2/3}$.

For example scaling the original bunch parameters R=*1* mm, L= *10* ps and solenoid B=0.31 T, to operation with reduced gun peak field, from 140 MV/m to 120 MV/m, one obtains R=1.1 mm, L=12.7 ps and B=0.27 T. The original, unscaled (continuous line) and scaled (dashed line) envelopes and emittances are shown in Fig. A8. This comparison seems to indicate that our scaling considerations work quite well.

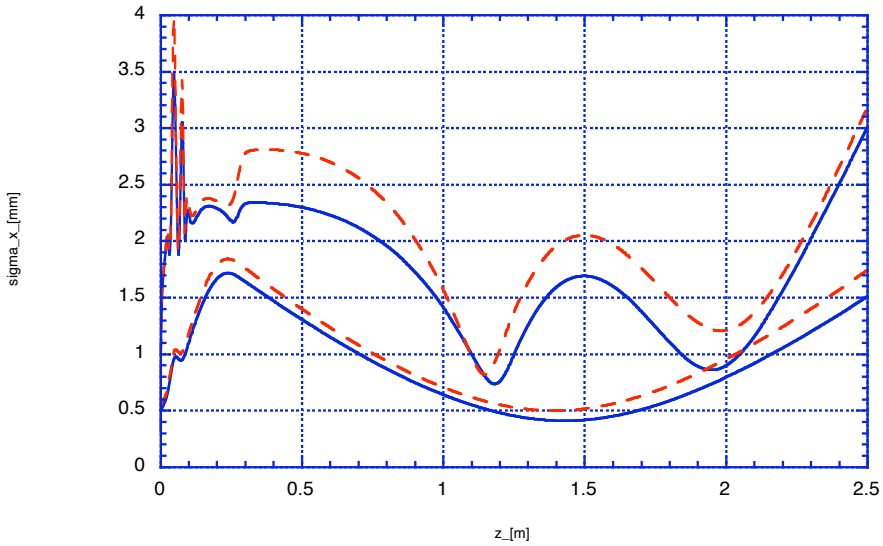

FIG. A8: Original (continuous line) and scaled (dashed line) envelopes and emittances

The theory of the invariant envelope has been a very important tool to clarify the emittance compensation process. In the next section we discuss how the concepts introduced in this section can be extended to the case of a bunch under the effect of a longitudinal focusing.

3.4 Start to end simulations

A start-to-end simulation of the beam dynamics from the injector through transfer line and undulator system has been performed by means of the codes PARMELA and GENENIS to quantitatively explore the expected performances of the injector systems in driving the SPARC FEL experiment. We take as our example the most conservative system that is to be encountered, one with no velocity bunching, and a relatively low energy of 155 MeV (consistent with either low gradient, three TW section operation, or high gradient, two TW section operation).

The transverse emittance compensation process is visible in Figure 3.2: the emittance reaches an absolute maximum in the centre of the solenoid and it is reduced to a minimum in the drifting section, then begins again to increase. The booster entrance is located at the envelope laminar waist corresponding to an emittance relative maximum. The emittance oscillation is driven by a properly matched accelerating field down to an absolute minimum (0.5 □m) at the linac exit where the average bunch energy is 155 MeV, high enough to damp space charge forces. The estimated thermal emittance (0.3 □m), included in the simulation, results to be in the present design the main contribution to the total emittance. As expected, the emittance along the transfer line and in the undulator is not anymore affected by space charge effect even when the beam has to be focused to a very small spot (~55 □m) to satisfy the undulator matching conditions. The total rms relative energy spread at the entrance of the undulator results to be less than 0.2 % as required The temporal profile of the bunch has been taken uniform over 11.5 ps

with a rising time of 1 ps, a laser spot on the cathode of 1 mm and a 1 nC charge, with a 35 degree launch phase in the gun, 0.27 T of solenoid field and on-crest acceleration in the linac.

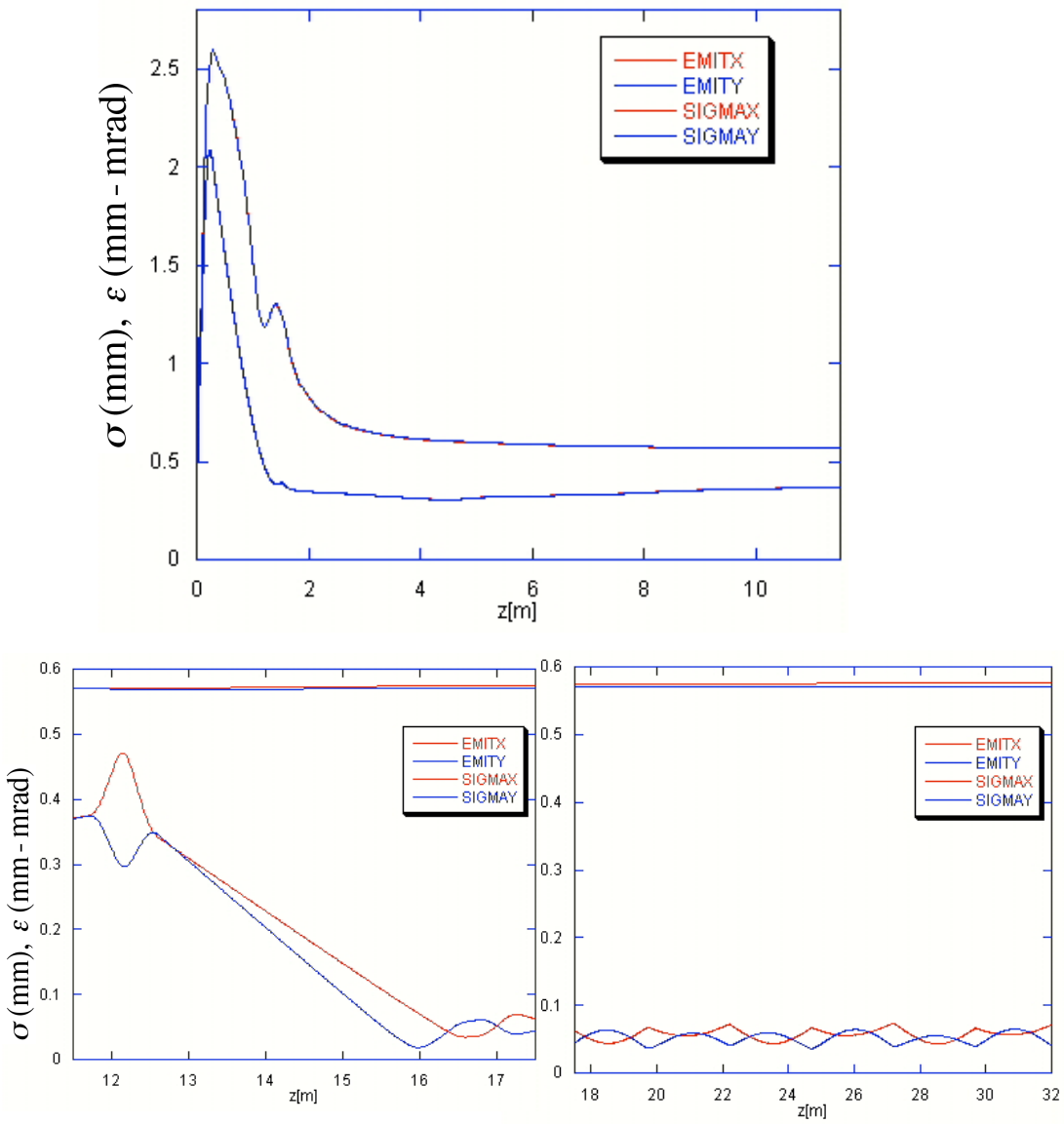

Figure 3.2. *PARMELA simulation of the rms normalized emittance and bunch envelope evolution along the SPARC beam-line, through the injector (to ~11.5 m), in the matching section (~11.5 to 19 m) and the undulator (past ~20 m).*

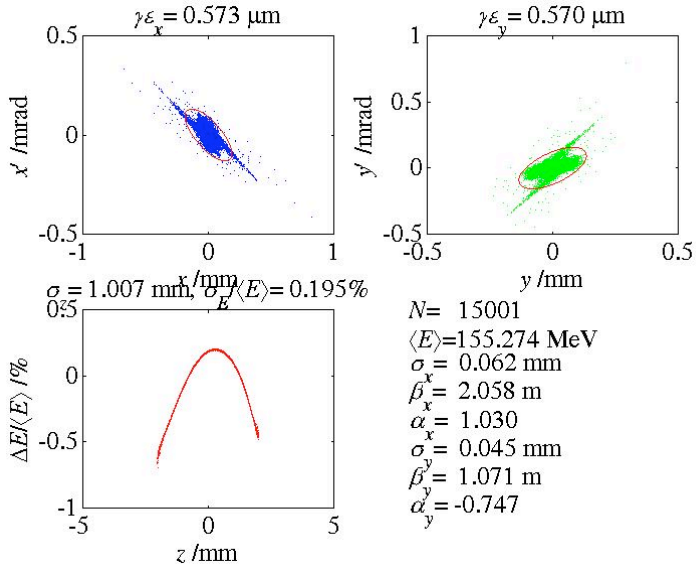

Figure 3.3: *Transverse and longitudinal phase spaces at the entrance of the undulator.*

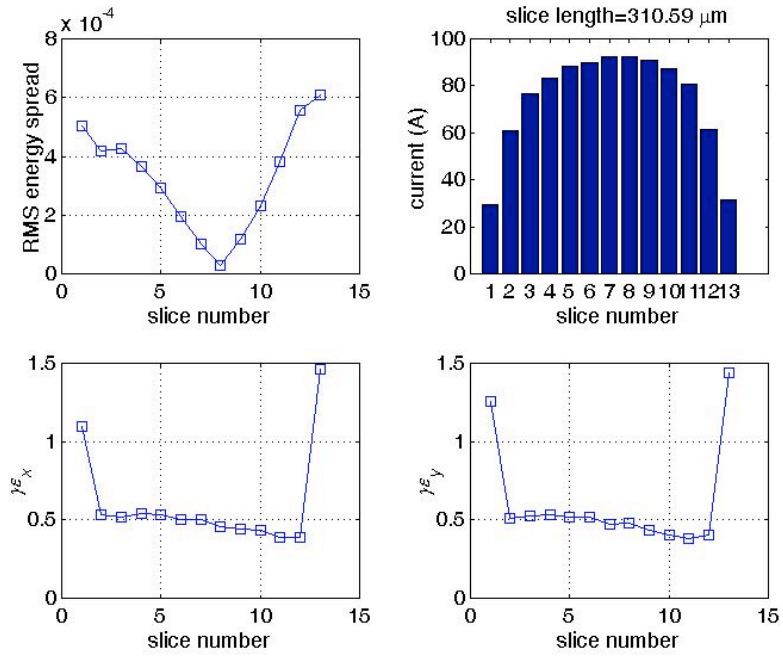

Figure 3.4: Slice analysis of beam properties at the undulator entrance.

In the simulations we have taken a conservative gun peak field of 120 MV/m resulting in a 5.6 MeV beam at exit of the RF gun. Matching such a beam to the linac by a straightforward application of Eq. (3.4) would result in an accelerating gradient of the first TW structure of 28 MV/m. We decided to use a more conservative gradient of 25 MV/m by increasing the focusing property of the first TW structure with a set of coils around the first accelerating structure (700 G), providing also additional flexibility in the choice of the gradient. To reach the transition energy given by (3.5) and to reach the design energy of 155 MeV another accelerating section operating at 25 MV/m would be enough. The third cavity is supposed to be a loan from SLAC (with an expected maximum gradient of 15 MV/m) and it will be mainly used for diagnostic purposes (slice emittance measurement). Nevertheless since the transport of the beam from the

exit of TW section two to the entrance of the undulator with section three turned off would require additional focusing, and since the gradients of the last two sections yield less sensitivity in emittance compensation dynamics, we decided to operate section two and three both at 12.5 MV/m to drive the FEL experiment, without any computed degradation of beam quality. At full energy mode (200 MeV) or in the slice emittance diagnostic mode we plan to operate the second TW structure at 25 MV/m and the third, which is rated for lower power, at 15 MV/m.

Transverse and longitudinal phase spaces at the entrance of the undulator are shown if Fig. 3.3. Despite some halo observed in the transverse phase space related to the bunch tails mismatch, the core of the bunch is very well behaved, having a 0.57 μm rms normalized emittance in both planes. The longitudinal phase space shows the typical energy phase correlation induced mainly by the RF field, with little contribution from longitudinal space-charge and wakes, having relative energy spread lower than 0.2% rms.

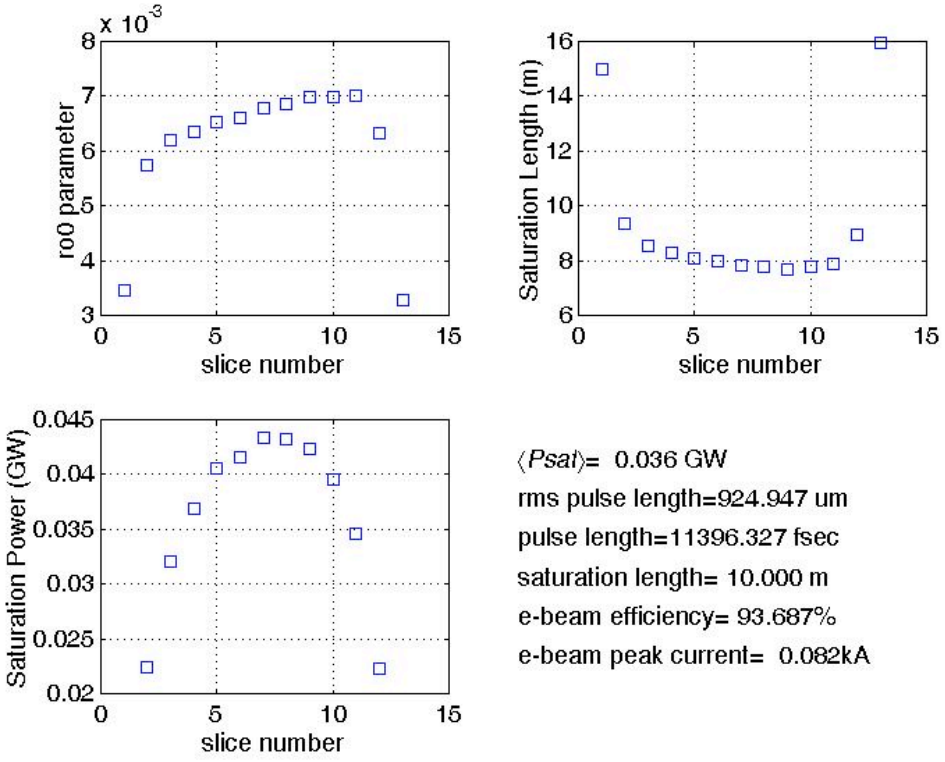

Figure 3.5: *Slice FEL parameters, saturation length and saturation power, according to Xie scaling laws.*

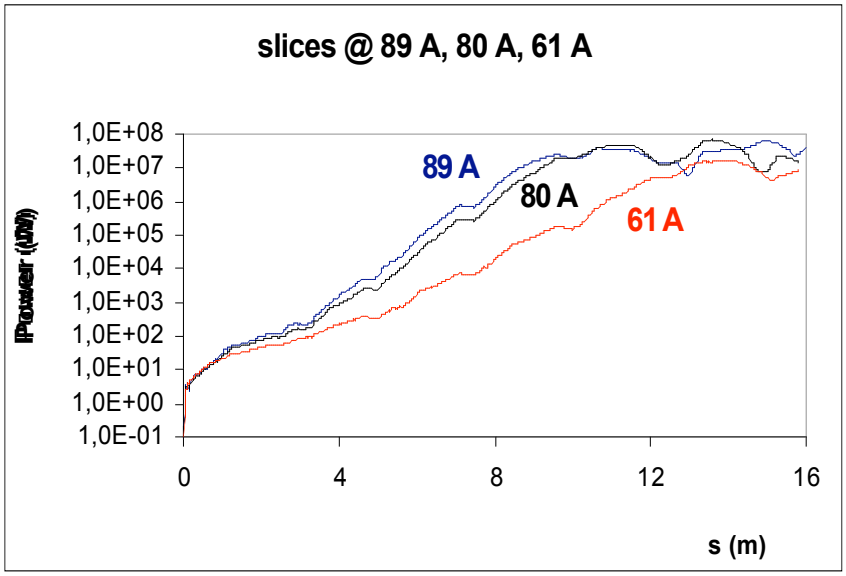

Figure 3.6: *GENESIS simulations of the FEL for three representative slices along the bunch.*

We recall that the relevant parameters for FEL operation are the slice emittance and slice energy spread[22], where the slice length is taken to be the FEL cooperation length, in our case 300 μm long (1 ps, or approximately 10 slices within the beam). The slice analysis performed at the undulator entrance is shown if Fig. 3.4. Slice emittance and energy spread are well below the nominal design values for more than 85% of the bunch length. The slice peak current is above 60 A in the same region. Simple scaling laws due to Ming Xie [23] predict that more than 70% of the bunch saturates in the 15 m long undulator as reported in Fig. 3.5.

A more careful analysis of the FEL performance has been performed with the code GENESIS, taking in to account three representative slices along the bunch provided by PARMELA. The agreement with the scaling law results, as displayed in Fig. 3.6, is very remarkable, showing that the even radiation emitted by the slices closer to the tails that contain a lower local value of the current (61 A) can reach saturation.

3.5 Parametric sensitivities

One of the major goals of the SPARC project is to experimentally explore the stability and robustness of the ultra-high brightness beam/SASE FEL systems. In order to appreciate how the performances of the systems are degraded by standard laboratory errors, jitters and uncertainties, one must analyze the systems with detailed models. In this section we discuss the results of such studies performed thus far, in which cathode emission uniformity, laser beam ellipticity, laser centroid offset, laser time structure, and solenoid field errors are explored. These studies are presently being expanded to include rf field amplitude and phase errors in a more systematic way [24].

3.5.1 Emittance dilution due to laser spot ellipticity

The goal of this analysis was to assess the effect on beam quality at low energy of an eccentric ($\sigma_x / \sigma_y \neq 1$) laser spot on the cathode. The simulations were made with the three dimensional TREDI Monte Carlo code run with $5 \cdot 10^4$ particles. Space charge effects have been estimated on a dynamic Cartesian grid of $20(n_x) \times 20(n_y) \times 30(n_z)$ points interpolating the values on the mesh to the positions of the particles. Emittance dilution as a function of $\eta = \sigma_x / \sigma_y$ (constant cross section) is shown in Fig.3.7. This study, which is intended as a support of the low energy (gun only) experiments in Phase 1a, shows that the beams may not be significantly out of round without causing a qualitative change in the emittance compensation dynamics. For $\eta = 1.2$, the emittance oscillation is qualitatively changed, losing its characteristic double minimum.

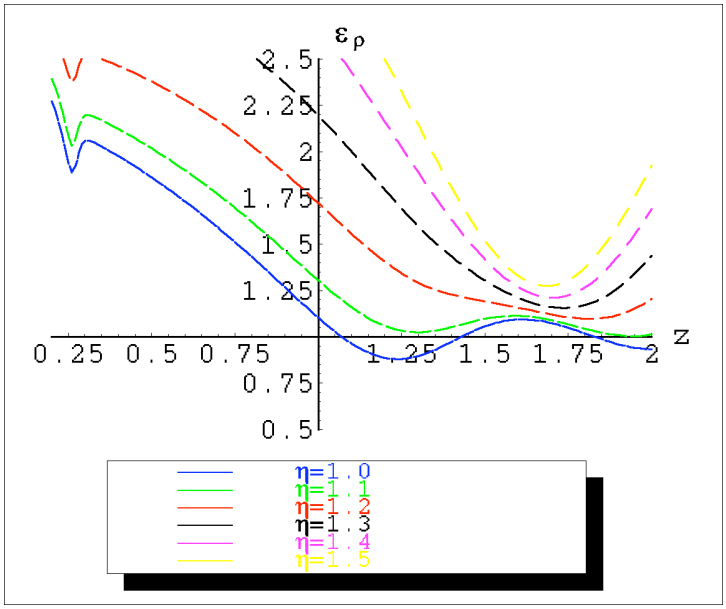

Figure 3.7 *Emittance dilution as a function of* $\eta = \sigma_x / \sigma_y$ *(constant cross section)*

A numerical study of the effect of the laser spot ellipticity on output beam emittance at high energy (Phase 1b) has been done using the PARMELA code. Calculations for an elliptical cross section input beam have been performed for different values of the ratio of the two semiaxes of the ellipse $\eta = \sigma_x / \sigma_y = X_{max}/Y_{max}$ in the range 1-1.6, keeping constant their product $\sigma_x \sigma_y = R_{cat}^2/2$ (R_{cat} = cathode radius = 1 mm) in order to preserve the beam density, and thus its plasma frequency, which controls the emittance oscillations (compensation). As the transverse ratio differs significantly from 1, the approximation used in the PARMELA 2D SCHEFF routine for the calculation of space charge for elliptical beams is no longer applicable and it is necessary to perform 3D calculations with a high number of particles (50K) using PARMELA 3D routine SPCH3D that does not assume any beam symmetry.

Figure 3.8 shows the plot of horizontal and vertical rms normalized emittance versus z up to the second TW section exit for different values of the η ratio. One can see that for η values

not larger than 1.1 the emittance compensation process still works in both planes, while for larger values the emittance control is lost.

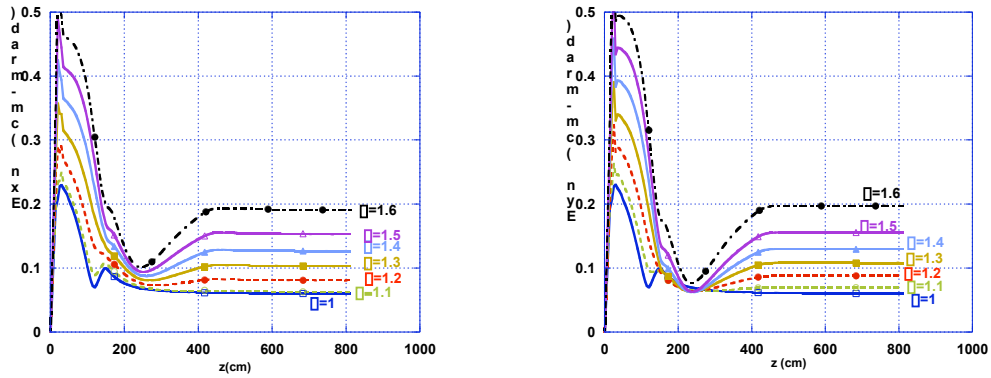

Figure 3.8 *Horizontal rms norm emittance (left figure) and vertical rms norm emittance vs z for different values of transverse eccentricity ratio .*

In Figs 3.9 and 3.10 the emittance growth at linac input and at the output of the first two SPARC accelerating sections is shown. One can observe that in the drift region after the gun the bigger increase in emittance occurs in the plane where the initial beam dimension is larger (*x*-plane), while after the traversal of the accelerating sections the greater increase occurs in the orthogonal plane (*y*-plane).

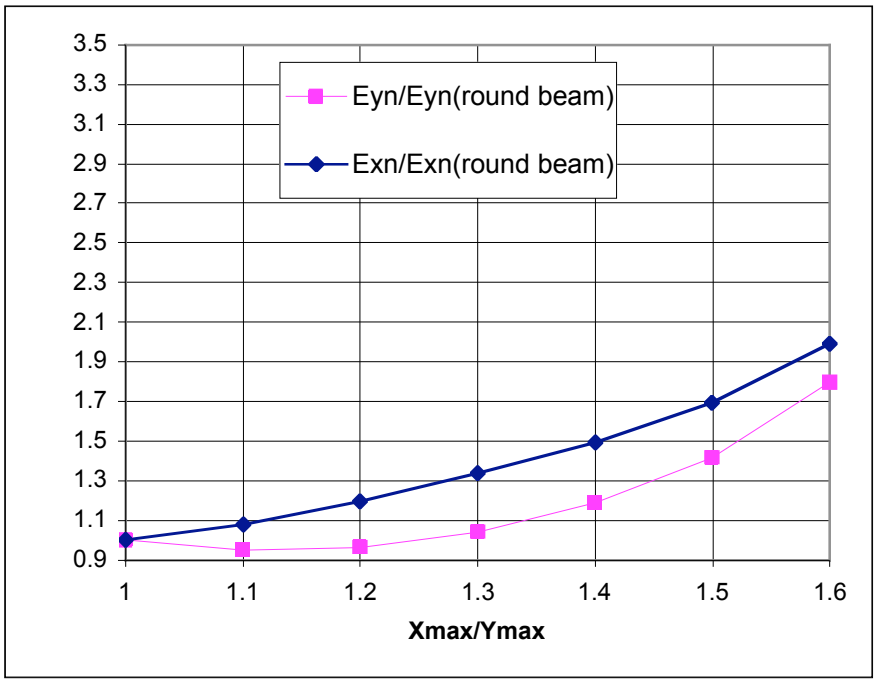

Fig 3.9 *RMS emittance growth at the linac input*

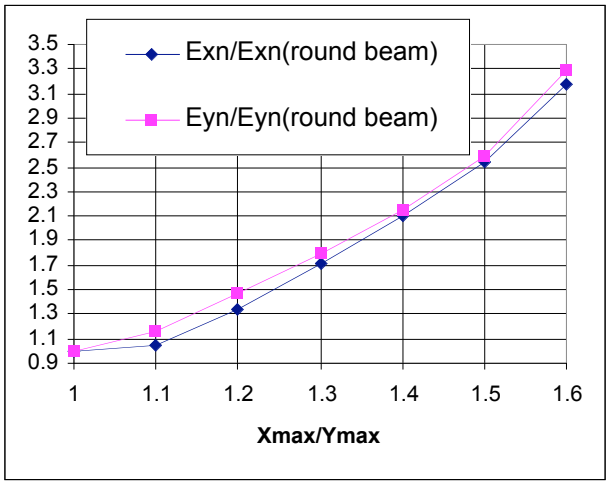

Figure 3.10: *RMS emittance growth at the second linac output*

This is due to the different entrance conditions and subsequent focusing in the structures as it is possible to see in Fig. 3.11 where the behavior of the horizontal and vertical envelopes is shown for = 1.5.

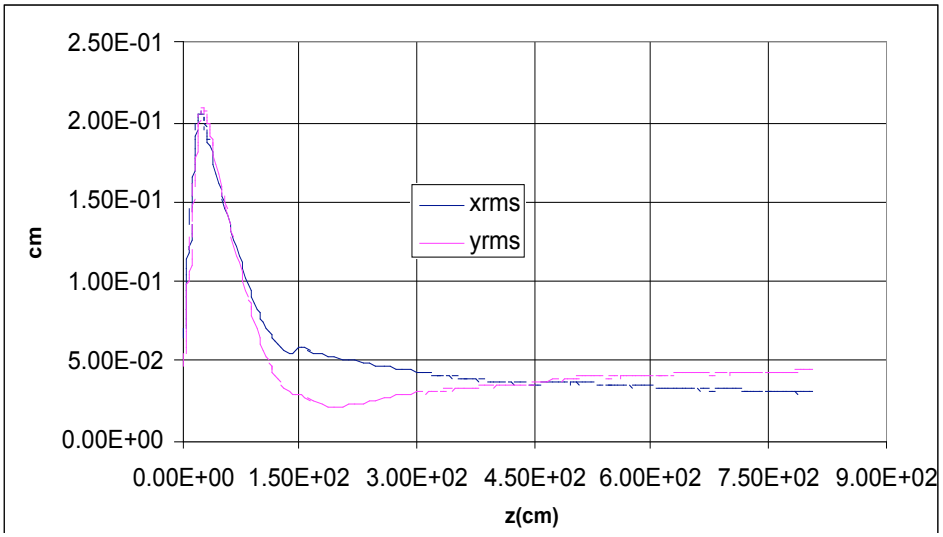

Figure 3.11: *RMS x-y envelopes versus z in the case of a transverse ratio 1.5*

From these results we can conclude that in order to keep stable control of the beam emittance in both planes and to limit the maximum emittance increase with respect to the symmetrical case to 15%, the transverse ratio of the laser spot should not to be larger than 10%.

3.5.2 Cathode emission inhomogeneities

The effects of cathode's inhomogeneities[25] have been tested by simulating, using TREDI's powerful 3D field calculations, a zone on the cathode with reduced quantum

efficiency. We assumed a circular spot (a "hole") with a surface S~10% (R~316 μm) of the nominal spot centered half-way of the spot nominal radius (x=0.5 mm, y=0.0 mm). Simulations were made as above ($5 \cdot 10^4$ particles, SC fields evaluated on a $20(n_x) \times 20(n_y) \times 30(n_z)$ 3D mesh) using the following parameter set: gun peak field E=140 MV/m, B=3.09 kG focusing solenoid strength, 10 ps laser pulse duration. Figures (3.12) and (3.13) show respectively the x-y space at extraction ($z = 0$) for $Q_E = 50\%$ and the emittance degradation as a function of Q_E. The results suggest that localized inhomogeneities do not dramatically degrade the emittance, for it grows by $\Delta\varepsilon_{x(y)} \approx 10\%(15\%)$ for $Q_E = 70\%$. This analysis will be further extended to the cases of randomly distributed ("spotty") inhomogeneities, which better describe the behavior of real cathodes.

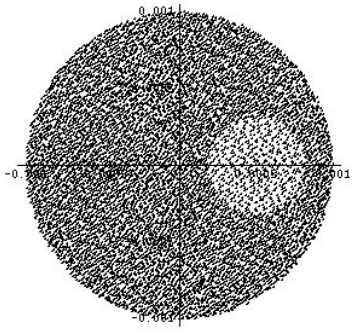

***Figure 3.12**: The x-y space at extraction (z=0) for $Q_E = 50\%$.*

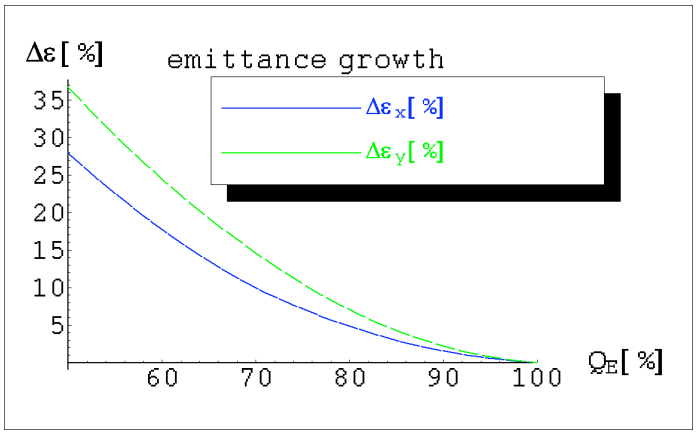

***Figure 3.13:** Emittance growth as a function of Q_E*

Apendix B: Analytical evaluation of emittance growth due to transverse non-uniformities.

An analytical evaluation of emittance growth due to transverse non-uniformities at the emission in RF guns can be done in the following way.

Following Kim, the two contributions of emittance growth for an electron beam produced in RF guns, are given, in the case of a cylindrical uniform charge density distribution (both in

radius and in time), by the space charge term $\Delta\varepsilon_n^{SC}$ and the RF term $\Delta\varepsilon_n^{RF}$. These specify the emittance dilution in the transverse phase space evaluated at the gun exit (hence in absence of any emittance correction mechanism)

$$\Delta\varepsilon_n^{SC} = \frac{Z_0 I}{64 E_0 \overline{\sin\phi}} \Delta_r(A)$$

$$\Delta\varepsilon_n^{RF} = \frac{\kappa^2 \kappa_1 R_{ex}^2 L^2}{3\sqrt{5}\lambda_{RF}^2}$$

where Z_0 is the vacuum impedance, $A \equiv \frac{R}{L}$ the laser pulse aspect ratio ($R \equiv$ laser spot size on the cathode, $L \equiv$ laser pulse length, assumed uniform in time), I the bunch peak current, $\kappa \equiv \frac{eE_0 \sin\phi_{ex}}{mc^2}$ is the accelerating gradient in the gun, E_0 the cathode RF peak field, ϕ_0 the launching phase at the cathode, ϕ_{ex} the exit phase, $\overline{\sin\phi} \equiv (\sin\phi_0 + \sin\phi_{ex})/2$, R_{ex} the bunch spot size at the gun exit (typically $R_{ex} \approx 2R$), λ_{RF} the RF wavelength and Δ_r a form factor approximately given by (for a bunch with uniform density in the radial and longitudinal directions)

$$\Delta_r(A) \approx \left(0.0306 A^{1/4} + 0.894\sqrt{A}\right) e^{-2.8A}$$

This is evaluated by a best fit of numerical results obtained by integrating HOMDYN linear space charge field form factor $G(z) = \frac{z/L}{\sqrt{(z/L)^2 + A^2}} + \frac{1 - z/L}{\sqrt{(1 - z/L)^2 + A^2}}$, and calculating emittance *a la Kim* by $\Delta\varepsilon_n^{SC} = \frac{Z_0 I}{64 E_0 \overline{\sin\phi}} \sqrt{\langle G^2 \rangle - \langle G \rangle^2}$ (hence the definition $\Delta_r(A) \equiv \sqrt{\langle G^2 \rangle - \langle G \rangle^2}$).

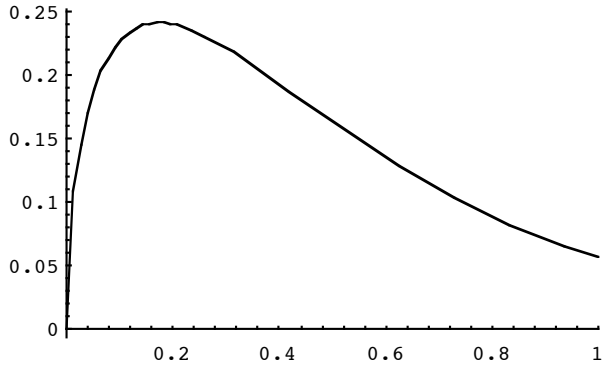

Figure B1 *form factor* Δ_r *as a function of laser aspect ratio* A *(solid line is the best fit of numerical calculations represented by the dots)*

The total emittance at the gun exit is given by

$$\varepsilon_n^{Kim} = \sqrt{\varepsilon_{th}^2 + \left(\Delta\varepsilon_n^{SC}\right)^2 + \left(\Delta\varepsilon_n^{RF}\right)^2}$$

where ε_{th} represent the thermal emittance contribution.

In the case of LCLS parameter set, i.e. $I = 100\ A\ ;\ E_0 = 120\ MV/m$, $R = 1\ mm\ ;\ L = 3\ mm\ ;\ \theta_0 = 30^0\ ;\ \theta_{ex} = 90^0$, and assuming $R_{ex} \cong 2R$ and a thermal emittance of $\varepsilon_{th} = 0.3\ mm \cdot mrad$, we obtain

$$\varepsilon_n^{Kim} = \sqrt{(1.5)^2 + (0.56)^2 + (0.3)^2} = 1.64\ mm \cdot mrad$$

Now we take a laser pulse displaying a radial non-uniformity in shape of an annular density corona, so that the bunch charge density distribution can be specified by

$$\begin{aligned} \rho &= \rho_0 && r < r_1 \\ \rho &= \rho_0(1+\delta) && r_1 < r < r_1 + \Delta r\ ;\ \Delta r << R \\ \rho &= \rho_0 && r_1 + \Delta r < r < R \end{aligned}$$

where Δr is the radial thickness of the annular corona, whose internal radius is r_1 (the laser edge radius is R).

The associated space charge fields, assuming very small laser aspect ratio (A<<1), are given by

$$E_{0r} = \frac{\rho_0}{2\varepsilon_0} r \quad r < r_1$$

$$E_{1r} = \frac{\rho_0}{2\varepsilon_0}\frac{1}{r}\left[(1+\delta) r^2 - \delta \cdot r_1^2\right] \quad r_1 < r < r_1 + \Delta r$$

$$E_{2r} = \frac{\rho_0}{2\varepsilon_0} r\left[1 + \frac{2 r_1 \Delta r (1+\delta)}{r^2}\right] \quad r_1 + \Delta r < r < R$$

Before calculating the emittance growth we must evaluate the density sheer caused by the radial expansion of the bunch due to the space charge field. Particles at the inner edge of the annular corona (i.e. at $r = r_1$) are pushed outward more than particles sitting at the outer edge of the corona for the case of a decreased density inside the corona itself. This makes inner particles to catch outer particles in the distribution, breaking the laminar flow and making the corona disappear, at least partially, by being filled with particles coming from inner radii.

To evaluate the radial motion in a perturbative fashion we start by calculating the radial momentum given by the space charge field on a particle traveling at a radius r (and position $L/2$ in the bunch) through the gun.

$$p_r^{SC} = \frac{mcZ_0 I}{2\pi R^2 E_0 \sin\theta_0} r \int_{\theta_0}^{\theta_{ex}} \frac{d\theta}{\sqrt{\left(\theta^2 - 1\right)\left(\theta^2 + 2A^2\right)}}$$

where ξ_{ex} is the value of ξ at the gun exit. The associated radial displacement of the particle, from the initial position r at the cathode and the exit from the gun (this is only the contribution of the space charge field) is

$$\Delta r = \frac{Z_0 I}{2\pi R^2 \varepsilon_0 \sin\varphi} r \int_1^{\xi_{ex}} \frac{d\xi}{\xi\sqrt{(\xi^2-1)(\xi^2+2A^2)}}$$

Assuming a very long bunch (i.e. $A \to 0$), the double integral can be well approximated, in the range of interest $5 < \xi_{ex} < 20$, by the formula $0.92\left(\xi_{ex}^2-1\right)^{1/4}$. Therefore, the difference $\delta(\Delta r)$ of radial displacement between particles leaving the cathode at radius r_1 and those at radius $r_1 + \Delta r$ (i.e. the inner and outer edges of the corona) will give us an indication on how much the corona density perturbation will be washed away through the gun.

$$\delta(\Delta r) = \frac{Z_0 I \Delta r\left(1+\dfrac{2r_1|\Delta|}{r_1+\Delta r}\right)}{2\pi R^2 \varepsilon_0 \sin\varphi}\left[0.92\left(\xi_{ex}^2-1\right)^{1/4}\right]$$

We will add therefore a damping factor $\eta \equiv e^{\frac{\delta(\Delta r)}{\Delta r}}$ to the following emittance growth calculations, that are performed *a la Kim* assuming a frozen bunch accelerated through the gun.

The emittance growth due to the non-linearity of this space charge field, induced by the variation of the density in the corona, is given by

$$\Delta\varepsilon_n^{cor} = \frac{Z_0 I}{8E_0\sin\varphi}\frac{r_1}{R}\sqrt{\frac{2r_1\Delta r|\Delta|}{R^2}}\eta$$

valid in the approximation $\frac{\Delta r}{R} << 1$, where $\eta = e^{-\frac{0.92 Z_0 I\left(1+2|\Delta|\right)\left(\xi^2-1\right)^{1/4}}{2\pi R^2 \varepsilon_0 \sin\varphi}}$.

The effect of a hole can be approximated by an equivalent surface corona, as in

$$\Delta\varepsilon_n^{hole} = \frac{Z_0 I}{8E_0\sin\varphi}\frac{r_1\Delta}{R}\sqrt{|\Delta|}\eta$$

where Δ is the hole diameter (hole center position is at r_1).

Taking again the parameter set of LCLS, and a corona whose inner radius is at $r_1 = R/2$, we obtain

$$\Delta\varepsilon_n^{cor} = 3.8\sqrt{\frac{\Delta r|\Delta|}{R^2}}\ \ mm\cdot mrad$$

implying $\Delta\varepsilon_n^{cor} = 1.04\ \ mm\cdot mrad$ for a 100 micron thick corona with 75% density variation in it. In this case $\frac{\delta(\Delta r)}{\Delta r} = 1.9$ so the corona is totally washed away (or even overcompensated) and the emittance damping factor comes out to be $\eta = e^{-1.9} = 0.18$. The total emittance will be thus distributed among basic space charge, RF, thermal and non-uniformity effects:

$$\varepsilon_n = \sqrt{(1.5)^2 + (0.56)^2 + (0.3)^2 + (1.04)^2} = 1.93 \ \ mm \cdot mrad$$

compared to 1.64 mm.mrad of the unperturbed case (no corona).

In case of a hole of diameter 100 micron, located 0.5 mm (R/2) off-axis, with 10% variation of the density in the hole, we obtain $\Delta\varepsilon_n^{hol} = 0.12 \ \ mm \cdot mrad$.

These evaluations must be taken as indicative of the emittance growth observed at the gun exit: the further emittance correction applied in the downstream drift space (as well as the acceleration in the first booster sections) typically reduces the total emittance down by a factor 3-4.

For this reason it is more relevant to specify the enhancement in the space charge induced emittance growth that one can expect from a transverse non-uniformity like a hole or an annular corona. The following are dimensionless coefficients predicting the emittance growth enhancement in the two cases:

$$\varepsilon^{cor} = \sqrt{1 + \left[\frac{8\Delta r_1}{\Delta_r(A)R}\sqrt{\frac{2r_1\Delta r}{R^2}}\right]^2}$$

$$\varepsilon^{hol} = \sqrt{1 + \left[\frac{8\Delta r_1 \Delta}{\Delta_r(A)R^2}\right]^2}$$

3.5.3 Sensitivity to Laser Rise Time and Time Structure

The electron beam's final characteristics strongly depend both on the spatial and on the temporal laser pulse shape. In order to optimize the characteristics of the electron beam, shaping of both phase and amplitude of the light pulse is required. We report in this section electron beam-dynamics simulations concerning the effects of temporal characteristics of the driving light pulse for optimal performances of the electron RF gun. The PARMELA code has been used for this analysis.

The studies on the temporal pulse shaping are particularly interesting. It is well known that the lowest beam emittance scan be obtained if the laser pulse is uniform in time, with short rise/fall times[26]. The simulations reported in Fig. 3.14 refer to a temporal pulse length of 11.65 ps FWHM, they show that the normalized projected emittance deteriorates as the laser pulse rise time increases. As results from these studies, flat top pulses with rise times shorter than1 ps are required in order to avoid emittance degradation.

As discussed in the upcoming laser section, laser pulse shaping with short rise time may result in the formation of longitudinal ripples. Therefore, the effect of a laser pulse with longitudinal ripples has been investigated and compared to a plain square pulse with no ripples. We have performed beam-dynamics simulations with a temporal pulse length of 11.65 ps FWHM, 1 ps of rise time and we have assumed the presence of ripples in the longitudinal distribution, having 10% and 30% of the nominal amplitude, as shown respectively in left and right plot of Fig. 3.15. The beam is assumed to be transversely uniform in these studies. The striking result is that even with a 30% of longitudinal irregularity the beam emittance does not appear to be strongly affected. This result is displayed in Fig. 3.16, where it is evident that the presence of ripples does not affect either the emittance or the rms beam envelope. This is clear also from Table 3.1, where the emittance value is moreover constant for the three reported cases.

This result can be interpreted as if the space-charge force induces a compensation of the longitudinal irregularity. This hypothesis is justifed by PARMELA simulation results. In Figs.3.17, 3.18, 3.19, 3.20 the longitudinal beam distributions along the beam line are displayed. At the cathode the temporal spectrum has a 30 % ripple overlapped on a square pulse, the relative energy spread is zero. As the beam goes through the gun and drifts the temporal oscillations transform in energy oscillations. At the entrance of the first acceleration structure (at z=150 cm) the beam has lost the temporal ripples, which have converted into energy variations through a fractional plasma oscillation. These energy ripples do not have any notable effect to the rms energy spread at the end of the linac, as they are soon suppressed inside the first accelerating structure.

These results indicate that the shape of the laser pulse should be square with a very small rise time, whether a smooth temporal profile is not a stringent requirement.

Table 3.1. *PARMELA simulation results: emittance after second RF accelerating structure versus longitudinal beam profiles.*

Beam distribution	emittance [mm mrad]
Square pulse 1ps rise time	0.580
Square pulse 1ps r.t. and 10% ripple	0.576
Square pulse 1ps r.t. and 30% ripple	0.616

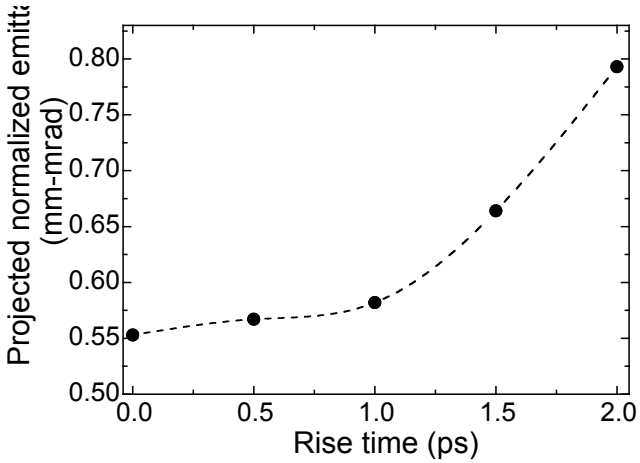

Fig. 3.14: *Normalized projected emittance vs rise time, calculated for thermal emittance of 0.3 mm and an electron beam of 1 mm radius (with uniform transverse distribution).*

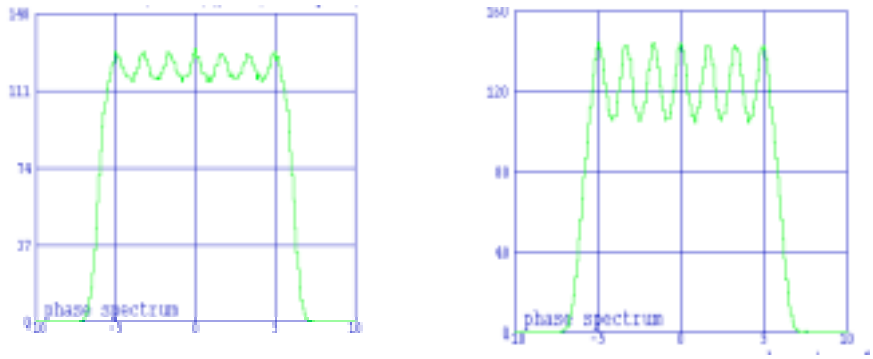

Fig. 3.15 *Longitudinal beam distribution with ripples, with 11.65 ps FWHM of temporal pulse length and 1ps of rise time. Left (right) plot: 10% (30%) amplitude irregularity.*

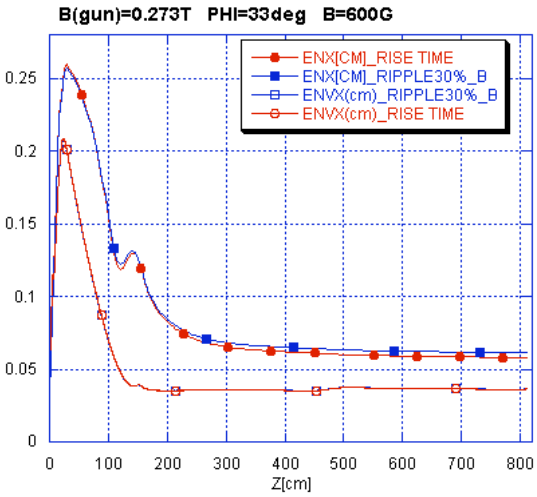

Figure 3.16 *Beam emittance and envelope with (blue squares) and without (red dots) 30% in amplitude longitudinal ripples: there are not significant changes for the two cases. These PARMELA simulations have been performed for a square pulse with 1ps of rise time , a solenoidal gun field of 0.273T, 33° RF of injection phase and solenoidal field at the first RF structure 600G.*

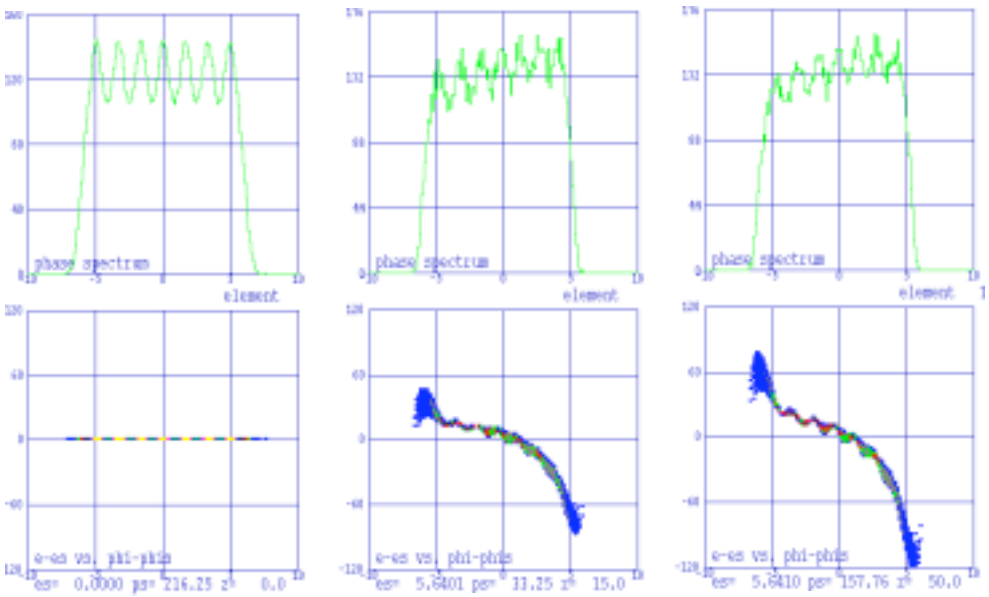

Figure 3.17*: Longitudinal beam distribution: phase and energy spectrum in the upper and lower plots, respectively. Left plot: initial distribution at cathode (z=0 cm); middle plot: at the end of RF gun (z=15cm); right plot: beam at z=50cm.*

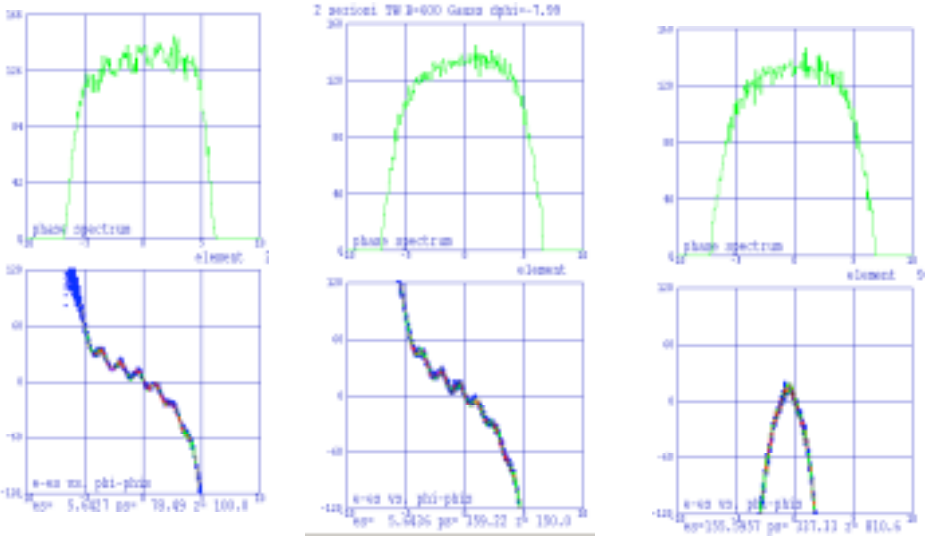

Figure 3.18: *Longitudinal beam distribution: First left plot: z=100 cm; second plot: at the entrance of first RF structure (z=150cm); right plot: at the end of second RF structure z=810cm.*

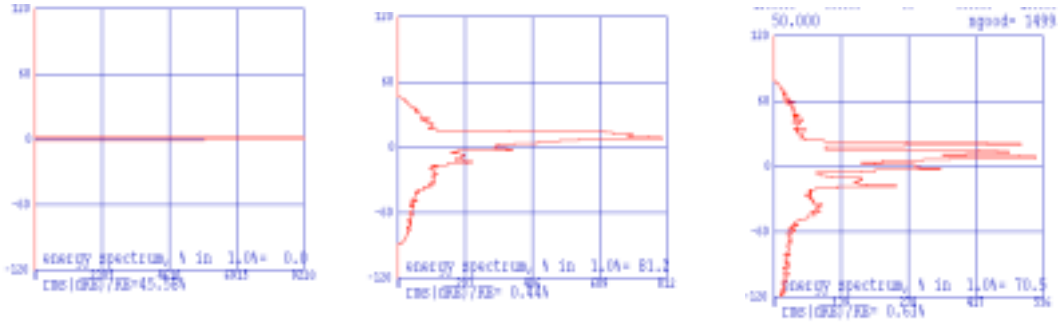

Fig.3.19: *Energy distribution at different longitudinal positions: Left plot: at cathode (z=0 cm); middle plot: at the end of RF gun (z=15cm); right plot: beam at z=50cm.*

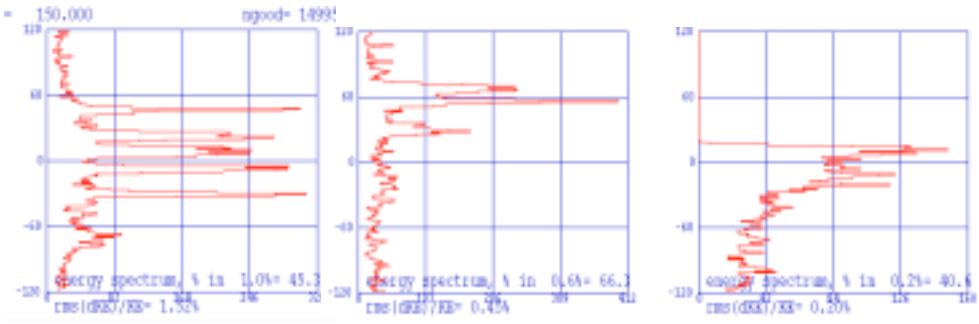

Figure 3.20: *Left plot: entrance of first RF structure (z=150cm); middle plot: energy oscillations at z=300cm; right plot: at the end of second RF structure, z=810cm.*

3.5.4 Sensitivity to phase jitter, gun solenoid field and first section solenoid field

Extensive computer simulations based on the PARMELA code have been performed in order to investigate the sensitivity of the beam projected emittance (also in dependence of the pulse rise time) to phase jitter, emittance compensating solenoid magnetic field and first section solenoid magnetic field.

In Fig.3.21 the variation of the output rms normalized emittance with the laser-to-gun phase is shown: in a range of phases between 31° and 34° the projected emittance growth is 4% for a uniform longitudinal distribution and rises to 6% for a 1 psec rise time pulse. From these results we can conclude that a tolerance of ±2° around the optimal phase is acceptable in order to limit the emittance growth to less than 10%. Figure 3.22 shows the dependence of beam projected emittance from the gun solenoid magnetic field intensity.

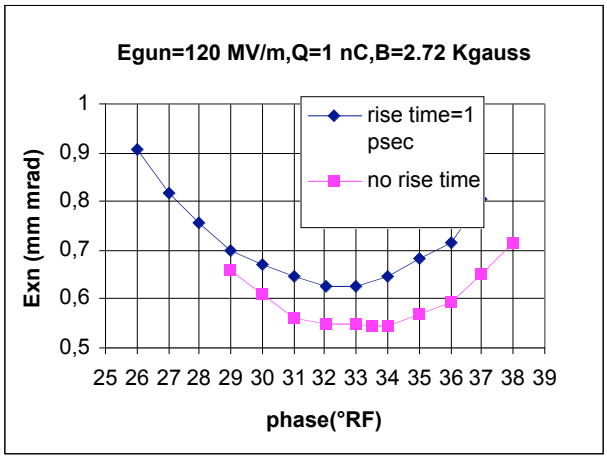

Fig. 3.21 *Projected rms norm. emittance vs gun phase*

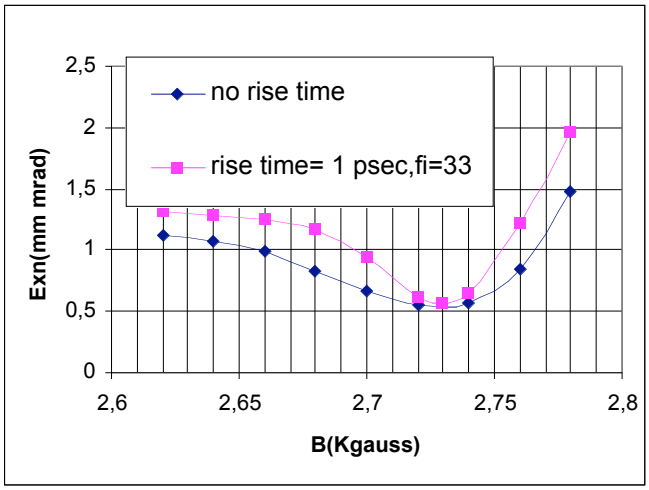

Fig. 3.22 *Projected rms norm. emittance vs gun solenoid magnetic field intensity*

It is noted that for a rise time of 1 psec, 1% variation of gun solenoid field value produces a 60% increase of the projected rms normalized emittance. However this high sensitivity is not a problem because a tolerance of 0.1% is achievable with the solenoid power supply, so the fine variation of the gun solenoid magnetic field coupled to an emittance measurement system placed at the end of accelerator can be used to tune the working point.

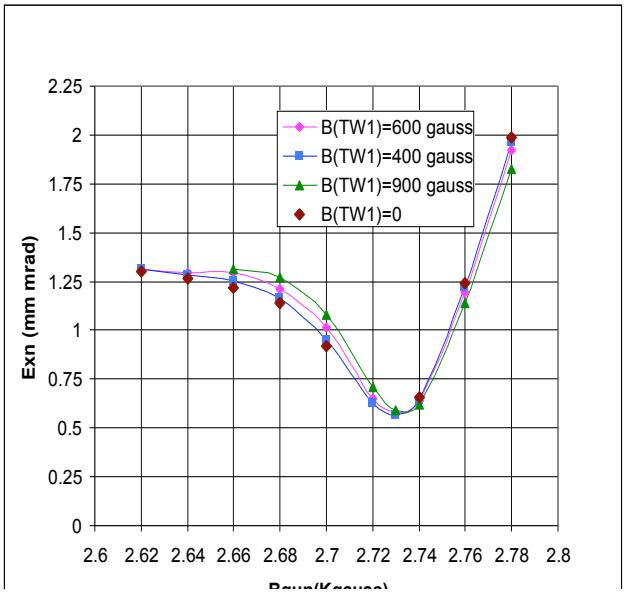

Figure 3.23 *Projected rms normalized emittance vs solenoid magnetic field for different intensities of the magnetic field produced by the solenoid on the first accelerating section*

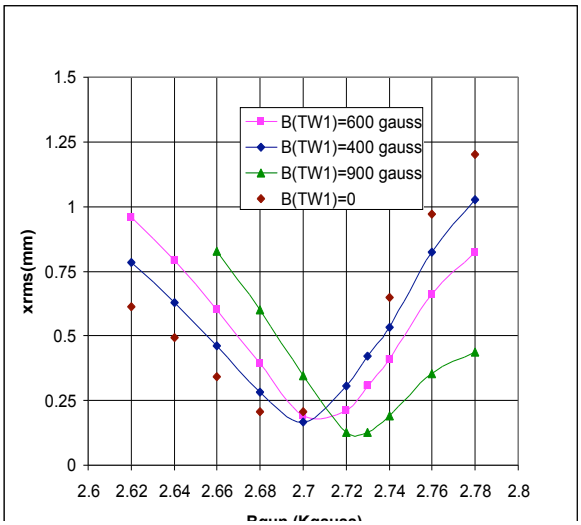

Figure 3.24 *Rms horizontal envelope vs solenoid magnetic field for different intensities of the magnetic field produced by the solenoid on the first accelerating section*

The plots shown in Figs. 3.23 and 3.24 refer to the effect of the first section (TW1) solenoid magnetic field amplitude. It can be noted that it has a very low influence on the final value of the emittance, while it has a great effect on the output beam size. Thus it may be employed to control the beam dimension and tune the Twiss parameters at the entrance of the transport line for an optimum matching with the undulator.

3.5.5 Sensitivity to Laser Pointing Stability

As discussed in the photocathode laser section below, the long optical transport line of the UV radiation from the laser room to the photo-cathode may produce a misalignment of the beam that gives rise to cathode illumination jitter. Simulations and experimental results at VISA FEL

(@600 nm) show that for optimal FEL performance the trajectory walk-off in the undulator should not exceed an rms beam size in a gain length [27]. In our case the rms beam size at the undulator entrance is 60 μm and the gain length is $L_g \sim 0.7$ m. The requirement of laser pointing stability less than 60 μm may not be the right answer, since the original beam offset could be magnified during the acceleration and transport along the transfer line (it would be in fact demagnified considerably if one naively employs linear optics analysis). The beam line is in fact optimized for a space-charge dominated beam dynamics while the centroid of the bunch behaves as a single particle. Because no space-charge force is acting on it, is "over-focused" by the emittance-compensating optics. In addition the beam divergence at the entrance of the undulator has to be less than 57 μrad to prevent walk-off in the undulator.

A preliminary study of this effect has been done by the code HOMDYN. In Fig 3.25 the beam envelope is shown along the beam line, from the gun up to the entrance of the undulator, together with the bunch centroid evolution for two different initial offsets: 33 and 100 μm. The initial centroid offset of 33 μm (100 μm) becomes a 40 μm (120 μm) at the undulator entrance.

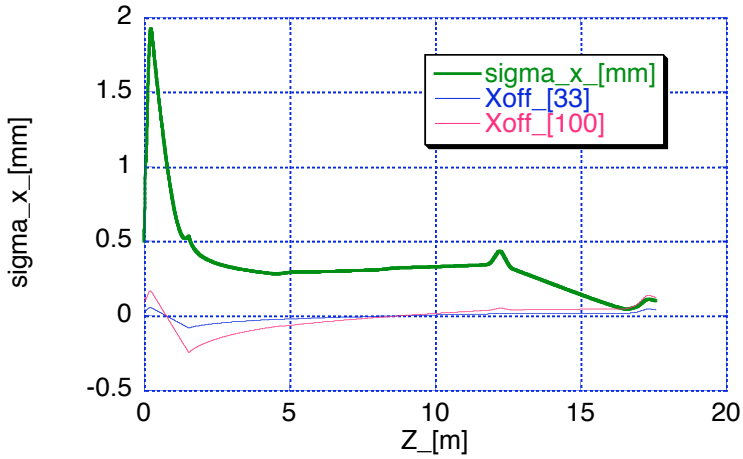

Figure 3.25: *Beam envelope and bunch centroid evolution along the beam line for two different initial offsets: 33 and 100 μm in the horizontal plane.*

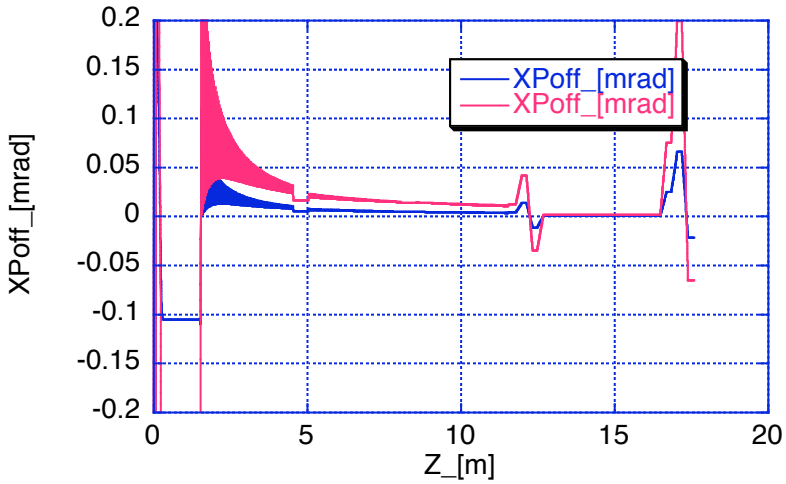

Fig. 3.26: *Beam centroid divergence X' along the beam line for two different initial offsets: 33 and 100 μm in the horizontal plane.*

As expected the betatron motion of the centroid and of the envelope are out of phase due to the differentiating effects of space-charge: the centroid cross the axis the first time at z=0.8 m while the beam envelope is gently focused to a space-charge dominated waist at the entrance of the first linac section. In the linac the focusing effect of the solenoid around the first accelerating section reduces the centroid offset, but when the beam leaves the linac the centroid still has an angle that is increased by the last triplet before entering the undulator. Figure 3.26 shows the beam divergence x[for the two cases along the beam line. The 33 □m (100 □m) offset case enters in the undulator with a 20 □rad (65 □rad) divergence. We can conclude that a laser pointing jitter of 30 □m is suitable for our purposes.

3.6 TRANSFER LINE DESIGN AND UNDULATOR MATCHNG OPTICS

The beam transport line (TL) is used to transport the electrons from the exit of the Linac (at z=11.5 m) to the undulator entrance. This part of the system is under the responsibility of ENEA, although the design is performed by a joint INFN/ENEA group. The TL must have enough flexibility to assure the transport of the beam, with emittance preservation, and the beam matching at the undulator input for the different injector operation scenarios, in particular, different energies. Due to the space available in the SPARC hall between the Linac and the undulator, the TL can be only 6 m long. The design must also provide enough space for the diagnostics (emittance and bunch length measurements) as well as for trajectory correcting coils and vacuum pumping system.

The TL magnetic layout is shown in Fig. 3.27. Two triplets are used to match the optical functions of the linac beam to the values desired at the undulator entrance. This solution, as opposed to a doublet and a triplet configuration which was also suitable, has been chosen in order to assure the most flexibility to the line. A 0.5 m free drift is left after the first triplet to allow for the possibility of installing a RF deflector for bunch length measurements and other diagnostics.

A small bending magnet will also be installed after the first triplet, and will be used for deflecting the beam through a 'dog-leg' line, for the measurement of the slice emittance, and through the by-pass where the magnetic beam compressor is foreseen in Phase II. This magnet has to be as close as possible to the first triplet, in order to assure enough clearance for the two beam lines, before the second triplet. In the present design, with 11° deflection angle at 200 MeV (maximum energy), there will be a 0.64 m space between the two beamlines. In Fig. 3.27 this bypass line is also sketched (drawing not in scale). The yellow triangle is the first dog-leg bend magnet, which is switched off for normal operation.

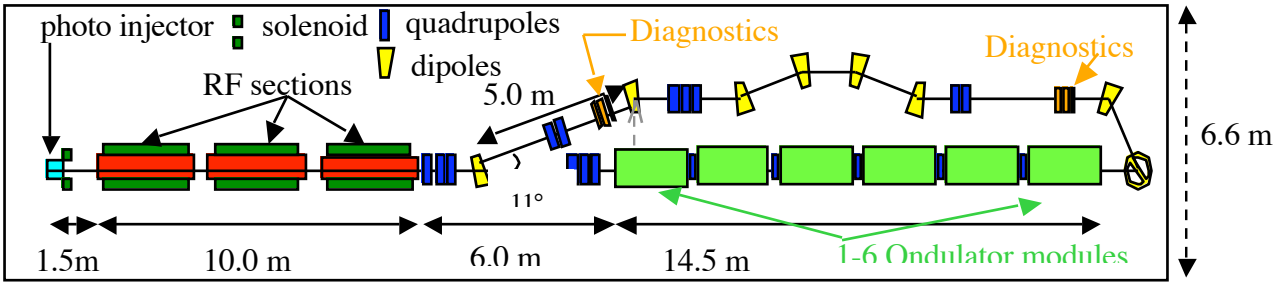

***Figure 3.27**: Sketch of the transfer line magnetic lay-out, from the linac exit to the undulator entrance (6 m total). Each quadrupole is 0.2 m long. The drawing is not to scale.*

Two cases have been studied at 155.3 MeV and 200. MeV, with correspondingly different values of the beam optical functions and emittance at the linac end. In Table 3.2 the beam the main TL parameters are summarized.

Table 3.2. – *TL characteristics*

Energy (MeV)	155. – 200.	**Max beam size (□)**	430. – 350.
Length (m)	6.0	**Max □$_x$ (m)**	110.- 80.
Number of 0.2 m quads	6	**Max □$_y$ (m)**	73. – 55.
Max quad strength (m^{-2})	10.	**Min □$_x$ (m)**	0.8 – 0.6
Max gradient (T/m)	6. – 7.	**Min □$_y$ (m)**	0.2 – 1.3

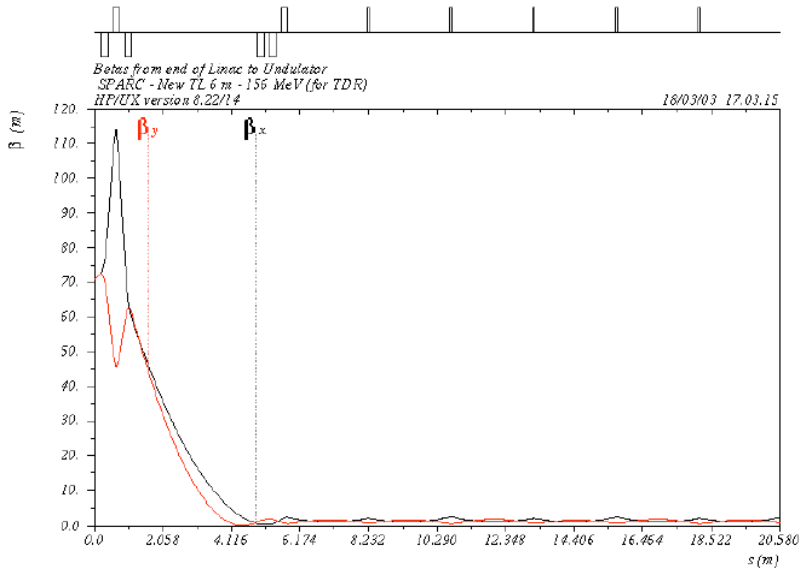

Fig. 3.28 *Optical functions in meters (black horizontal, red vertical), for the 155 MeV case, from the Linac output to the undulator output (z=0. corresponds to 11.5 m from the gun).*

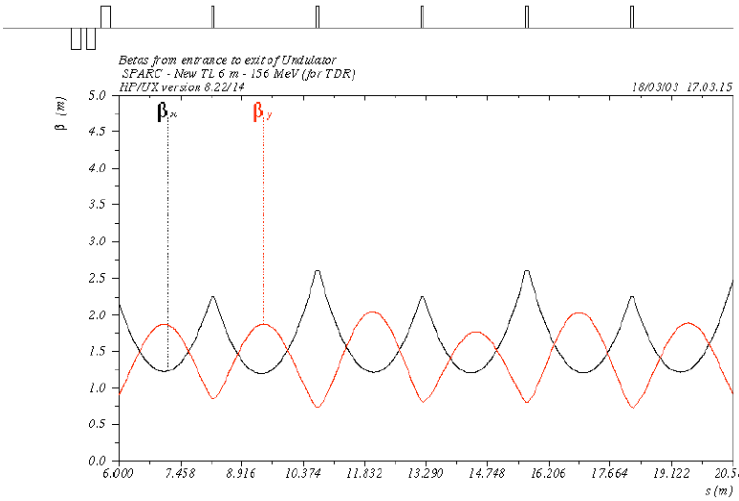

Fig. 3.30 *– Detail of the optical functions (black horizontal, red vertical) for the 155 MeV case, inside the undulator.*

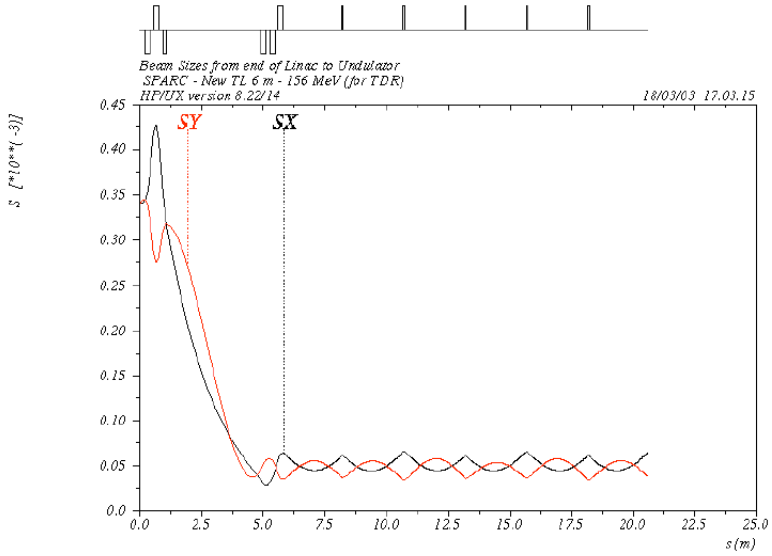

Fig. 3.40 *– Beam sizes in mm (black horizontal, red vertical) for the 155 MeV case. The normalized beam emittance is 500 mm.*

In Fig. 3.28 the behaviour of β_x and β_y from the end of the linac (corresponding to z = 0 in the plot) to the undulator input is plotted. The details of the evolution of β_x and β_y in the undulator is plotted in Fig. 3.29 on an expanded scale. The peak horizontal beam size, see Fig. 3.30, ranges from 430. to 350. m in the TL. The matching has been done including the focal effects of 6 undulator sections interleaved by small horizontally focusing quadrupoles. The effect of each undulator section on the beam has been simulated as a vertically focusing quadrupole.

The magnetic layout and quadrupole strengths for the 155 MeV case are summarized in Section 3.7, for the TL and the first undulator section (repeated 6 times). In both cases, 155. and 200 MeV, the average value in the undulator is between 1.3 and 2. m. A start-to-end simulation with PARMELA, with and without space charge effects, has shown no effect on the beam emittance due to beam transport in Phase I, even in presence of such a small minimum values as those achieved in the TL at the second triplet. With the higher currents foreseen in Phase II, it is anticipated (and observed in preliminary simulations) that one must take care to control the residual emittance (plasma) oscillations that will occur in the presence of enhanced space-charge forces.

3.7 SIMULATION PARAMETER LISTS

In order to provide a compact reference to the simulation inputs for the numerical work involved in the present SPARC beam dynamics design, we provide here a listing of the most relevant parameters employed in this work.

GUN

Charge	1	nC
Longitudinal pulse form	trapezoidal *	
FWHM e-beam duration	11.7	psec
Rise time	1	psec
RMS thermal emittance	0.3	mm-mrad
RF frequency	2856	MHz
Number of cells	1.6	
Maximum extraction field	120	MV/m
Electron beam energy at exit	5.64	MeV
Phase**	33	°
Solenoid field	2.73	Kgauss
Solenoid centre	0.19	m

** stack of 15 gaussians*
*** cathode at z=0*
**** phase of the bunch centre*

LINAC

Number of sections	3	
Section length	3	m
First section solenoid field (a stack of 11 Helmoltz coils)	750	Gauss
First section accelerating field starting point	1.5	m
Position of the centre of the initial cell of the first section	1.535	m
Drift between the sections	0.5	m
First section solenoid field starting point	1.4	m

	Final energy = 156.6 MeV (λ_{FEL} 500 nm)	Final energy = 200.2 MeV (λ_{FEL} 290 nm)
First Section accelerating field	25 MV/m	25 MV/m
Second Section accelerating field	12.5 MV/m	25 MV/m
Third Section accelerating field	12.5 MV/m	15 MV/m
First section phase	(on crest)	(on crest)
Second section phase	(on crest)	(on crest)
Third section phase	(on crest)	(on crest)

Beam parameters (*linac output*)

Output energy	156.6 MeV	200.2 MeV
Peak current	85 A	85 A
RMS Energy Spread	0.2 %	0.2 %
RMS Transv. Norm. Emittance	0.6 mm mrad	0.6 mm mrad
RMS Longitudinal Emittance	980 deg-KeV	1246 deg-KeV
β_z	1 mm	1 mm
β_x	0.4 mm	0.3 mm
β_{xy}	71 m/rad	53 m/rad
α_{xy}	- 4	- 2

Slice parameters (*linac output*)

Slice length	300	μm
Slice energy spread	0.05	%
Slice RMS norm. emittance	0.5	mm-mrad

TRANSFER LINE

Element	L_{tot} (m) from Gun	Strength (m^{-2}) @ 155 MeV	G (T/m) @ 155 MeV	Strength (m^{-2}) @ 200 MeV	G (T/m) @ 200 MeV
Drift	11.7	-	-	-	-
Q1	11.9	-3.86	-2.	-3.75	-2.5
Drift	12.05	-	-	-	-
Q2	12.25	7.74	4.	7.63	5.1
Drift	12.4	-	-	-	-
Q3	12.6	-4.42	-2.3	-4.46	-3.
Drift	16.4	-	-	-	-
Q4	16.6	-7.67	-4.	-6.10	-4.1
Drift	16.75	-	-	-	-
Q5	16.95	-7.65	-4.	-5.80	-3.9
Drift	17.1	-	-	-	-
Q6	17.3	9.78	5.1	8.51	5.7
Drift	17.5	-	-	-	-
Und Sec	19.63	-0.9412	-	-0.5727	-
Drift	19.69	-	-	-	-
QF	19.75	14.43	7.5	9.72	6.5
Drift	19.99	-	-	-	-

Total length= 6 m

UNDULATOR

Number of modules	6
Module length	2.13 m
Period	0.03 m
Magnetic length	12.78 m
Break length	0.36 m
Number of breaks	5
Effective length	14.58 m
Gap	11 mm
K	2
q-pole length	6 cm
Drift before q-pole	6 cm
Drift after q-pole	24 cm
q-pole strength / gradient for E= 156.6 MeV ((β_{FFI} 500 nm)	K^2 = + 13. 85508 m^2, G= 7.215 T/m
q-pole strength / gradient for E= 200.2 MeV ((β_{FFI} 290 nm)	K^2 = + 10. 30248 m^2, G= 6.8683 T/m

MATCHED TWISS PARAMETERS AT UNDULATOR ENTRANCE

Energy (MeV)	155.3	200.
γ^{norm} (mm mrad)	0.5	0.6
β_x (m) Und IN	2.05	2.26
α_x Und IN	0.86	0.6
β_y (m) Und IN	1.02	1.52
α_y Und IN	-0.62	-0.54

3.8 MODELLING OF DIAGNOSTIC SYSTEM BEAM DYNAMICS

The goals of the SPARC injector project require that sophisticate modeling and diagnostic approaches be undertaken jointly, in support of each other — the bench-marking of codes with experiments, and the illumination of the underlying beam dynamics by simulation. We now present some results of detailed modeling of concerning two of the more elaborate experiments planned for the SPARC injector program, the low energy slit-based emittance measurement, and the high energy dispersion-based slice emittance measurement.

3.8.1 Low energy emittance measurement simulations

The first phase of the SPARC project consists of the commissioning of the low energy section of the photoinjector system (5.6 MeV beam), with a systematic measurement of the emittance compensation process during the post-rf gun drift. This systematic study is intended to learn as much as possible about the critical low energy portion of the compensation process, where the emittance oscillations are most pronounced, and there is thus more risk in handling the beam. The most serious anticipated sources of non-ideal behavior in emittance compensation arise from non-uniform beam emission at the cathode, due to laser or photoemitter imperfections. To study the low-energy emittance compensation process in detail, before the areas needed for both propagation and diagnosis are occluded by a linac section, a dedicated, movable (in z) emittance-meter tool has been proposed for this phase. More aspects of this device, schematically shown in Fig. 3.31, are discussed further in the diagnostic section of this document.

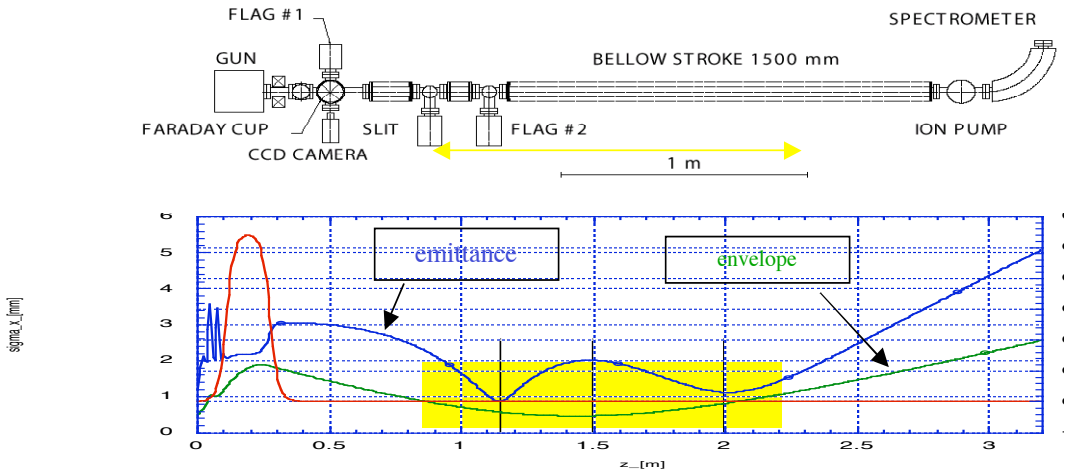

Figure 3.31: *Movable emittance measurement tools (upper picture); rms normalized emittance and envelope evolution from the cathode to the drift end (lower picture). The solenoid field (red line, lower plot) is also shown, and the yellow area represents the range of the movable emittance measurements.*

The emittance measurement in the drift after the SPARC photocathode gun will be based on the multislit technique, in which the beam is sliced into well-separated sampling beamlets by means of an intercepting mask (Fig. 3.32). The slits convert the space charge dominated incoming beam into several emittance-dominated beamlets that then drift to a detection screen. The intensity of beamlet spots on the screen is directly proportional to the number of particles in the beamlets which hit the screen. Numerical simulations of the measurement based on PARMELA beam dynamics calculation have been done in order to verify the optimization the

device's mechanical measurement assembly parameters (slit width and spacing, distance between multislit mask and output screen) which may be chosen on the basis of analytical guidelines [28]. The simulations also serve to evaluate the effect of the residual space charge which has been minimized by the correct choice of the design parameters. They also check the possibility of retrieving the rms emittance in the range of interest.

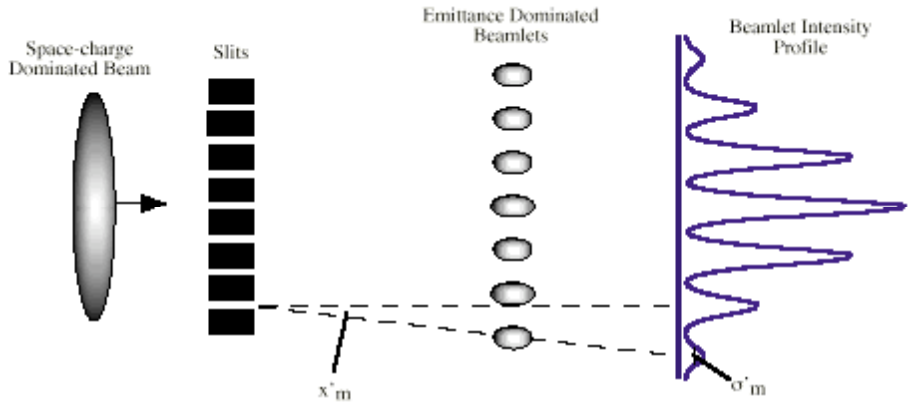

***Figure 3.32**: Multi-slit based emittance measurement scheme*

In particular, we have developed two MATLAB-based programs. The first one generates a simulated output image by means of a density plot generated from the phase space distribution predicted by PARMELA, which is used to retrace each electron from before the slits up to the output screen. The second MATLAB program retrieves the phase-space parameters from the simulated image recorded by the first program on a TIFF file.

The formula used to find the rms emittance [29] employs only geometrical parameters of the slits and of the spots on the screen:

$$\varepsilon_n^2 = \langle x^2 \rangle \langle x'^2 \rangle - \langle xx' \rangle^2$$
$$= \frac{1}{N^2} \left[\sum_{j=1}^{p} n_j \left(x_{sj} - \bar{x} \right)^2 \right] \left[\sum_{j=1}^{p} n_j \sigma_{x'j}^2 \right] + n_j \left(\overline{x_j} - \bar{x} \right)^2 \left[\sum_{j=1}^{p} n_j x_{sj} \overline{x'_j} - N \bar{x} \overline{x'} \right]^2 \qquad (3.6)$$

where:

p = total number of slits
n_j = number of particles passing through j-th slit and hitting the screen (this is a practical weighting of spot intensity
x_{sl} = slit positions
x_j = mean position of spots on screen
x = mean position of all beamlets
x_j =mean divergence of all beamlets
σ_j = rms size of spots on screen

The first step of the numerical simulation of the emittance measurement is the beam dynamics calculation in the SPARC region gun + drift. The plot of Fig. 3.33 shows the normalized rms emittance and rms x-envelope computed by PARMELA in this region. The temporal distribution of the 1 nC input beam is given by a pulse with a 11.7 psec width (FWHM) and 1 psec rise

time, while the radial distribution is uniform. The particle coordinates are saved in a binary file along the drift at steps of 5 cm in order to have the possibility to introduce at different points of the drift an intercepting multi-slit mask, simulated by cutting the output PARMELA distribution. The surviving particles are traced in a successive run from the "cutting" point (the mask plane) up to the output screen.

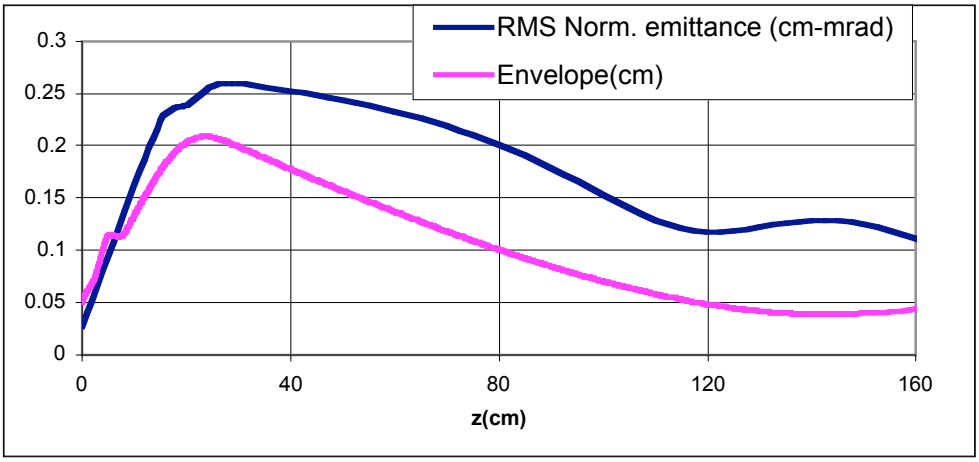

Figure. 3.33: *RMS normalized emittance and RMS x-envelope in the gun+drift region computed by PARMELA (N_p=450K).*

For the simulation of the emittance measurement we begin with 450K simulaiton particles, in order to save, after the cut, a number of particles that can be sufficient for the successive computation that requires a large number of particles (50K at least), if one wants to take into account the residual space charge effect, noting that a 3D calculation is needed being the beamlets a collection of sheet beams.

Analytical considerations based on the envelope equation [6] applied to the SPARC beam (I 100 A, 0.5 mm, $_{msn}$ 1 mm-mrad) yield a slit width d< 75 m in order to have an emittance dominated beam expansion after collimation. The slit spacing w has to be chosen much larger than the slit width and smaller than the beam size to ensure that the beam can be resolved ($d < w <$). The drift length L between the slit plate and the output screen is a compromise between two considerations; it must be large enough to have a high resolution for the low beam emittance, but small enough to prevent the overlapping of the beamlet profiles on the screen.

The following parameter set has been used: d = 65 m, w = 300 m, L = 20 cm. In the case of a measurement setup with these parameters about 74K particles survived the intercepting slits. These particles are re-input to PARMELA for the tracking to the output screen. Figure 3.34 shows the *x-y* plot of PARMELA distribution computed before and after the multi-slit mask, while Figure 3.35 shows the *x-y* plot of PARMELA distribution computed on the output screen and the relative image obtained by an intensity plot recorded in a TIFF format file.

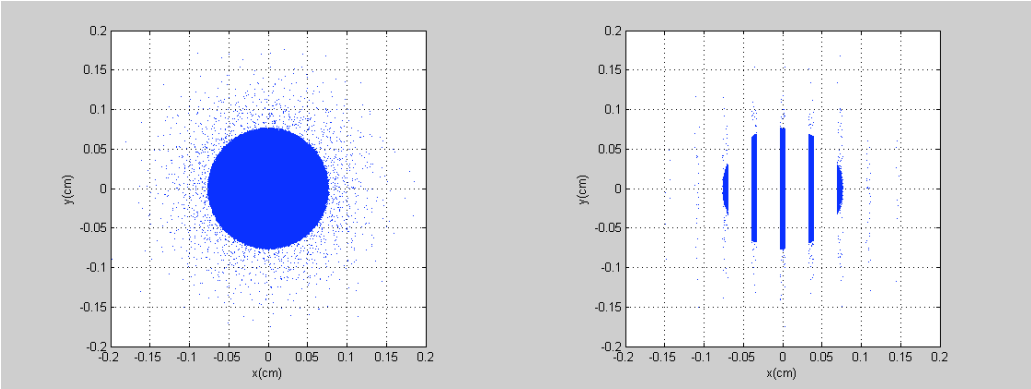

***Figure 3.34*:** *Spatial x-y plot of PARMELA distribution at z=150 cm before the slits (Np=450K) and immediately after the zero thickness slit (Np=74671)*

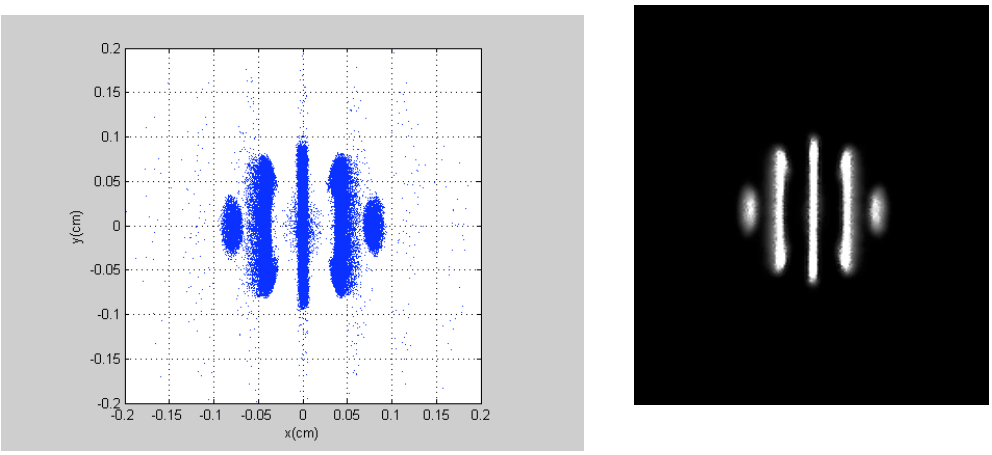

Figure 3.35: *Spatial x-y plot of PARMELA distribution at z=170 cm and the relative image reconstructed on the output screen*

The image file has been acquired and analyzed by a MATLAB based program that retrieves the intensity distribution of the beamlets and computes the rms emittance (non normalized) and the Twiss parameters. The relative output is presented in figure 3.36 showing the screen image, the reconstructed intensity distribution, the computed beam ellipse and the retrieved phase – space parameters. Using the same approach we span the *z*-region around the beam waist between 120 and 150 cm from the cathode.

In Fig. 3.37 and Table 3.3 the PARMELA values of the rms un-normalized emittance are compared with the values obtained simulating the multi-slit mask using the phase distribution predicted by PARMELA. The calculations were done in all cases switching off the space charge in the region from the mask plane to the output screen. The maximum error in this region is 7%. Only in one point (z=150 cm) we repeated the calculation with the space charge on, in order to estimate the error due to the residual space charge. The increase of the measured emittance is negligible, around 1.4%.

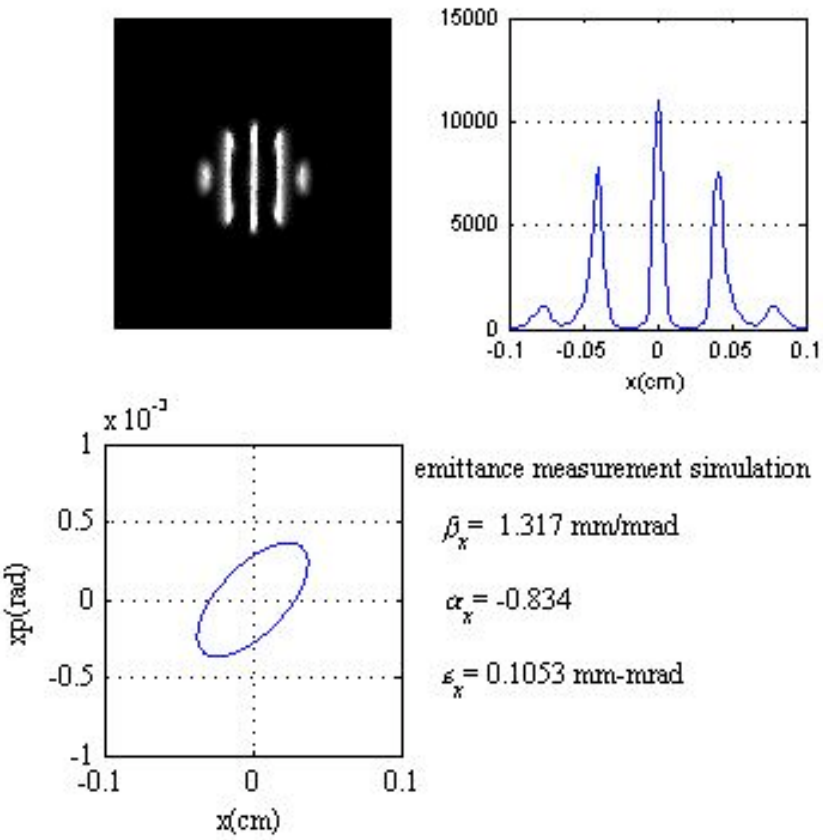

Figure 3.36 *Output of the MATLAB program analysing the PARMELA distribution on the output screen(L=20 cm).*

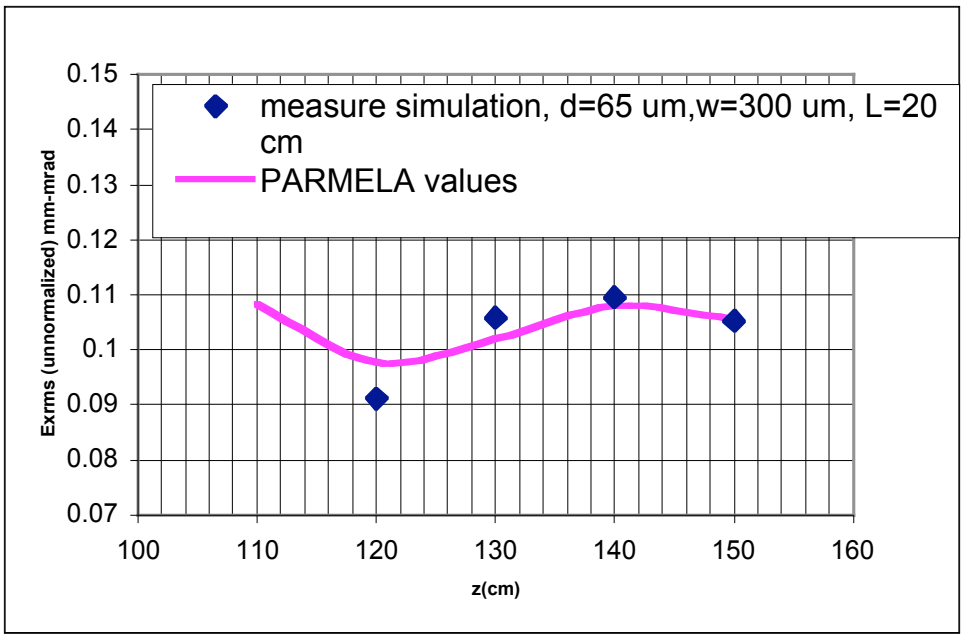

Figure 3.37 *RMS geometrical (un-normalized emittance) vs z.*

TABLE 3.3

z (cm)	ε_{rms} (mm mrad) (PARMELA value)	ε_{rms} (mm mrad) (retrieved value from virtual measure) *space charge off*	ε_{rms} (mm mrad) (retrieved value from virtual measure) *space charge on*
120	0.0977	0.0912	
130	0.102	0.1058	
140	0.108	0.1095	
150	0.1055	0.1053	0.1068

3.8.2 Wake field effects in the bellows

When the emittance measurement slit array is shifted downstream the drift, the beam must propagate inside an increasingly longer bellows assembly. The bellows' convolutions generate wake fields that may affect the measurement results by degrading the beam's emittance and the energy spread [30]. In this section we briefly discuss a study of the wake-fields induced in the bellows. An analytical model [31] due to Bane and Sands is compared with numerical simulations made with the code ABCI, and a preliminary evaluation of the wake-induced effect is presented.

The analytical model (based on pill-box corrugations) for the bellows impedance uses the following geometric notation: g is the corrugation length, a is the beam pipe radius, b is the corrugation depth. The maximum extension of the bellows envisioned in the experiment is 1.5 m with more than N_t~400 corrugations.

For a uniform distribution charge the longitudinal and transverse loss factors per period are:

$$k_{\|} = \frac{4}{3\sqrt{2}} \frac{Z_0 c}{\pi a^2} \sqrt{\frac{g}{l}} \quad \left[\frac{V}{C}\right] \tag{3.7}$$

$$k_{\perp} = \frac{2^{\frac{7}{2}}}{15} \frac{Z_0 c \sqrt{lg}}{\pi^2 a^3} \quad \left[\frac{V}{Cm}\right] \tag{3.8}$$

The formulas showed above were obtained for one convolution. The total bellows wake is not simply the summation of all individual convolution wake; the wakes combine to reduce their individual wake as the beam moves along the bellows as

$$k_N = k \frac{2}{1+\sqrt{N}} \quad , \tag{3.9}$$

where k_N is the loss factor longitudinal or transverse for one convolution. Equation (3.9) is correct until the bunch reaches the N_{eq} convolutions, where

$$N_{eq} = \frac{a^2}{2g(\pi + \frac{2a}{\pi})}. \tag{3.10}$$

From this convolution to the end of the bellows, the individual wake remains equal to the N_{eq} wake and the cumulative wake increases linearly with N, so the loss factor for all bellows is given by:

$$k_{tot} = \left[\sum_{n=1}^{N_{eq}} \frac{2}{1+\sqrt{n}} + \frac{2(N_t - N_{eq})}{1+\sqrt{N_{eq}}} \right] k \tag{3.11}$$

The plots in Fig. 3.15 represent the loss factor for two different longitudinal distributions: a Gaussian bunch and a uniform distribution bunch. It compares analytical formula of Eq. 3.38 with results obtained with simulations made with the code ABCI for a Gaussian bunch and a squared and triangular shaped bellows. Excellent agreement is obtained between theory and numerical results, especially for the case of a Gaussian bunch.

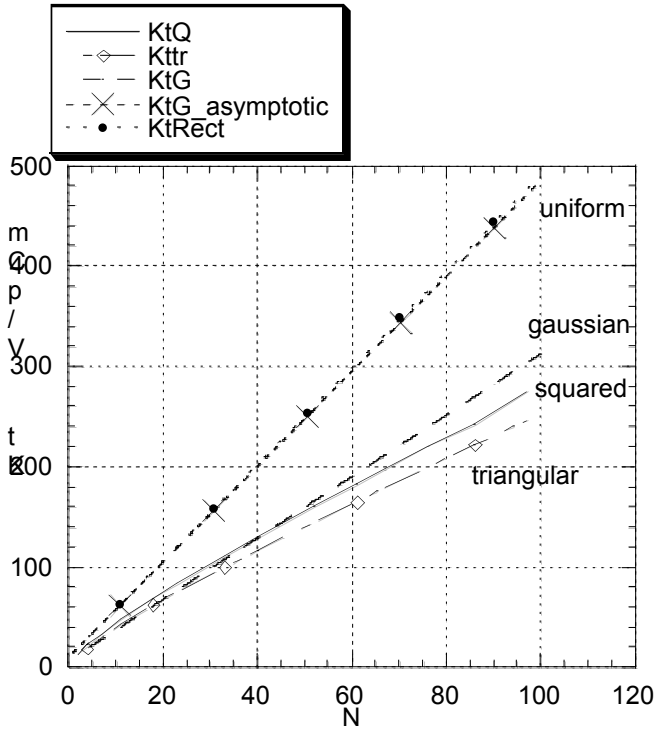

Figure 3.38: *Comparison between the transverse loss factor versus the number of convolutions, obtained with the code ABCI for a triangular and squared bellow and the analytical formulas of a Gaussian bunch. The plot represents also the transverse loss factor of a uniform bunch and a Gaussian bunch using the asymptotic analytical expression. The bellows being used has dimensions: a=1.6cm, b=2.5cm, g=0.5cm (extended). The bunch rms length is σ=1mm.*

Note that equation 3.18 for a gaussian bunch is quite close to the numerical simulation, whilst the case of a uniform bunch almost coincide with the asymptotic equation of a gaussian bunch.

These results have been used to examine some different choices of the bellows proposed for the SPARC project. For example, we may take a bellows with the following dimensions: *a*=51.25 mm, *b*=75 mm, *g*=0.90 mm (compressed) - 4.40 mm (extended), corresponding to 340 corrugations. The induced energy spread in case of maximum extension of the bellows in this case is high, around 1.2%.

The second choice results to be more effective to damp wake-field effects. Notice that the induced energy spread in case of maximum extension of the bellow of case two is of the order of 1.2%, the same order of the space-charge induced energy spread. The emittance degradation corresponding to these effects will be soon evaluated with an improved version of HOMDYN. As to transverse effects, we can make an estimate for the moment by comparing the transverse space charge force with the transverse wake force for experimental conditions. It is found that the transverse wake for any reasonable offset is much smaller than the transverse space charge force at the edge of the beam, indicating that one may expect wake-fields to not interfere strongly with measurement of emittance compensation after the gun in Phase 1a.

3.8.3 High energy slice emittance simulations

The beam will be accelerated up to the final nominal energy 155 MeV by the three traveling wave structure and transported up to the undulator entrance in SPARC Phase 1b. Measurement of slice emittances after final compensation in the linac sections, will be at this stage one of the main experiments to do in view of obtaining the best FEL performances We discuss in this section the slice emittance measurement virtual experiment.

The emittance compensation with a solenoid field relies upon the alignment of the relative phase-space orientation of each temporally slice of the electron bunch. The high brightness beam in the gun occurs when the time sliced-emittance is nearly the same as the cathode thermal emittance and when the slices have nearly the same Twiss parameters. The measurement of the slice emittance is then a powerful tool for verifying and tuning the photoinjector performance.

The slice emittance is the transverse emittance of a short time interval (slice) of the microbunch. It can be measured using an energy-dispersed beam with a linear energy-time correlation or chirp. The chirp is then combined with the quadrupole scan technique to determine the emittance of the slices along the bunch [32,33,34].

In Fig. 3.39 the channel section involved in the measurement is shown: the third linac section is de-phased to produce the desired chirp. After the first triplet, a dipole deflects the beam into the test-line and a screen is placed at the dispersion maximum location. The first two quads after the linac sections are used for the quadrupole scan: the beam is scanned vertically while keeping the horizontal betatron function and thus the horizontal betatron beam size constant. The vertical beam size is measured at the screen vs the doublet strength variation to obtain the emittance of the beam.

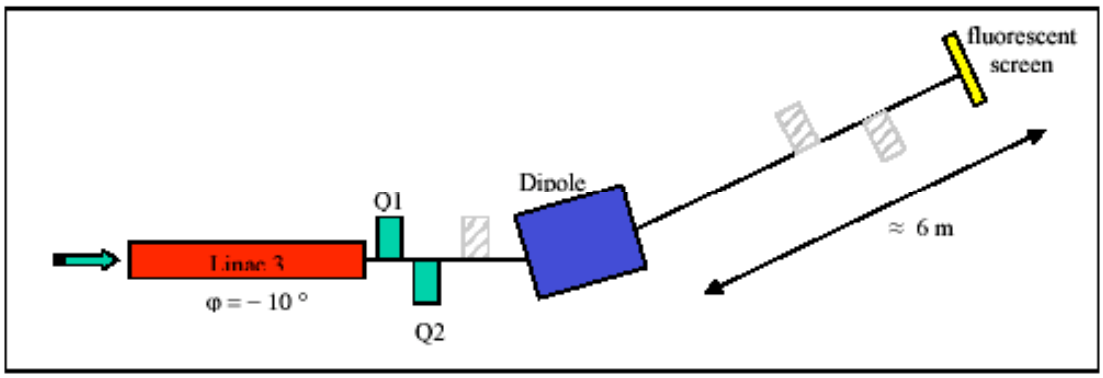

Fig. 3.39: *Schematic layout of the slice emittance measurement set-up.*

The beam particles in the two-dimensional phase space are surrounded by the phase ellipse described by:

$$\gamma x^2 + 2\alpha xx' + \beta x'^2 = \varepsilon \tag{3.12}$$

where, α, β, γ are the Twiss parameters and ε is the beam emittance.

The equation of an ellipse can be written in the form:

$$\boldsymbol{u}^T \sigma^{-1} \boldsymbol{u} = 1, \tag{3.13}$$

where $\boldsymbol{u}$ and $\boldsymbol{u}^T$ are the coordinate vector and its transpose and σ is a symmetric matrix.

For the ellipse equation in the two dimensional case we get:

$$\sigma_{11} x^2 + 2\sigma_{12} xx' + \sigma_{22} x'^2 = 1, \tag{3.14}$$

and comparison with (3.22) defines the beam matrix by

$$\sigma = \begin{pmatrix} \sigma_{11} & \sigma_{12} \\ \sigma_{12} & \sigma_{22} \end{pmatrix} = \varepsilon \begin{pmatrix} \beta & -\alpha \\ -\alpha & \gamma \end{pmatrix} \tag{3.15}$$

from which we have

$$\sigma_{11}\sigma_{22} - \sigma_{12}^2 = \varepsilon^2. \tag{3.16}$$

By measuring the beam size under different focusing conditions, different parts of the ellipse will be probed by the beam size monitor and the beam emittance can be determined through fitting of the data.

In matrix formulation the ellipse parameters transform from a starting point $s = 0$ to any other point $s \neq 0$ by the transformation:

$$\begin{pmatrix} \sigma_{11} \\ \sigma_{12} \\ \sigma_{22} \end{pmatrix} = \begin{pmatrix} R_{33}^2 & -2R_{34}R_{33} & R_{34}^2 \\ -R_{33}R_{43} & (R_{33}R_{44} - R_{34}R_{34}) & -R_{34}R_{44} \\ R_{43}^2 & -2R_{44}R_{34} & R_{44}^2 \end{pmatrix} \begin{pmatrix} \sigma_{11} \\ \sigma_{12} \\ \sigma_{22} \end{pmatrix}_0 \tag{3.17}$$

where $\mathbf{R}$ is the transport matrix from 0 to s. If we want to determine the beam matrix at a point P_0, we consider downstream a beam transport line up to a beam size monitor , e.g. a fluorescent screen, and we have for the beam size at the screen location,

$$\sigma_{11} = R_{33}^2 + 2R_{34}R_{33}\sigma_{12} + R_{34}^2\sigma_{22}. \tag{3.18}$$

By varying the focusing of the transport line, we have for each focusing condition and the relative beam size measurement at the screen :

$$\begin{pmatrix} \sigma_{1,11} \\ \sigma_{2,11} \\ \vdots \\ \sigma_{n,11} \end{pmatrix} = \begin{pmatrix} R_{1,33}^2 & 2R_{1,33}R_{1,34} & R_{1,44}^2 \\ R_{2,33}^2 & 2R_{2,33}R_{2,34} & R_{2,44}^2 \\ \vdots & \vdots & \vdots \\ R_{n,33}^2 & 2R_{n,33}R_{n,34} & R_{n,44}^2 \end{pmatrix} \begin{pmatrix} \sigma_{11} \\ \sigma_{12} \\ \sigma_{22} \end{pmatrix} \tag{3.19}$$

Fitting of the parameters β_{11}, β_{12} and β_{22} to match the measured curve, the beam emittance can be determined from (3.16). To measure the slice emittance each beam picture collected at the screen is "sliced" along the horizontal axis, and for each slice the beam size is determined for each different focusing condition of the line. The emittance of each slice is then obtained fitting the beam matrix parameters for each measured curve.

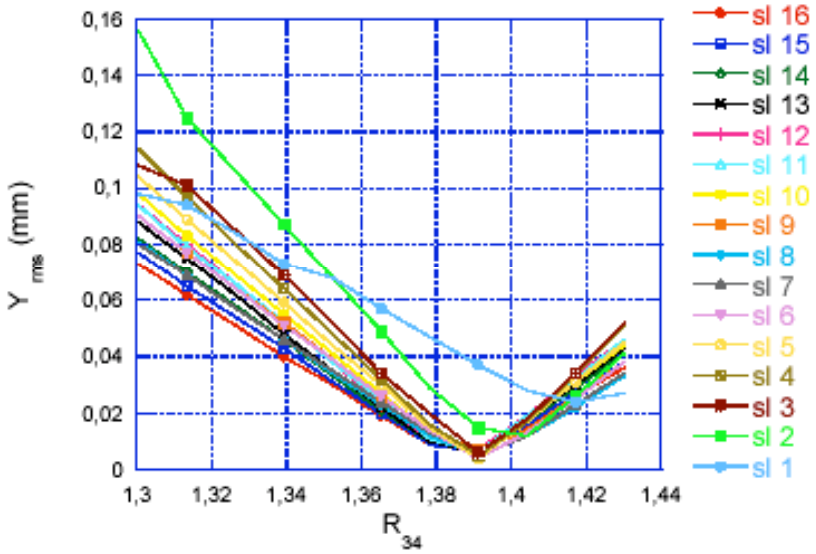

Figure 3.40. *Quadrupole scan results: the vertical beam size is reported vs. the transport matrix element* R_{34}

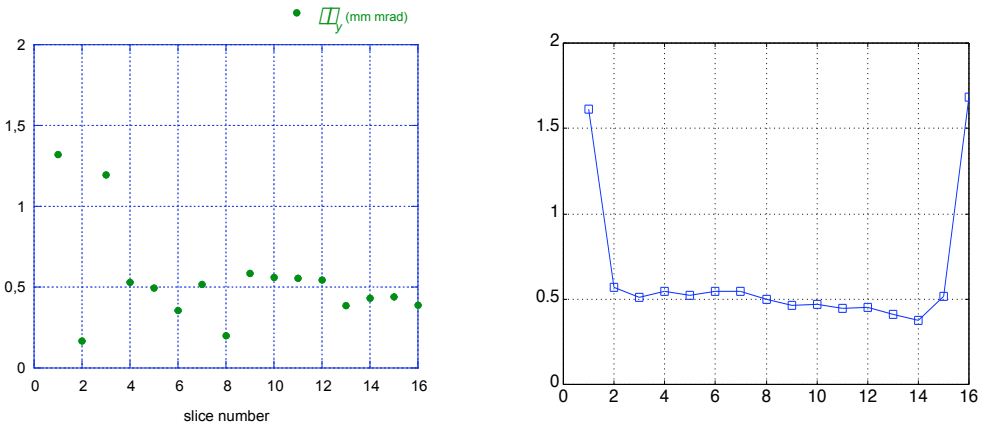

Figure. 3.41 *The results of the quadrupole scan simulation are reported in figure a). The time analysis of the unperturbed beam is shown in fig b).*

The slice emittance measurement has been simulated with the ELEGANT code; the first results are reported. The 15k particles beam obtained with PARMELA, at the end of the second linac section, is tracked into the third one with a phase delay of 10 deg and a reduction of energy less than 1 MeV. For each set of the doublet upstream the deflecting dipole, the final distribution of the beam, as collected on the screen, is analyzed. With the help of a Matlab code the x-y distribution is divided into 16 slices equally spaced along the horizontal axis; for each slice the vertical rms size is determined. In Fig. 3.40 the results of the quadrupole scan is reported for each slice.

The three parameters σ_{11}, σ_{12} and σ_{22} are obtained by fitting the curve; the emittance is obtained with the (3.16), the results obtained for each slice are reported in Fig. 3.41. a). In Fig. 3.41. b) the time analysis of the unperturbed beam is reported for comparison. Further simulation work is in progress for the measurement setup tuning, in order to achieve the best conditions for the resolution and precision of the results. It is notable that the simulated virtual measurement does not automatically produce accurate results (*e.g.* when the beam envelopes of all of the slices are not measured about both sides of the minimum in the variable parameter), and in doing so gives us insight into how to avoid errors in the actual measurement.

3.9 HIGH PEAK CURRENT EMITTANCE COMPENSATION (PHASE 2)

SPARC Phase 2 will be mainly devoted to beam dynamics studies related to bunch compression systems. Two possible schemes will be compared, as shown in Figure 3.42. A standard magnetic chicane will be installed in a parallel beam line, while a new technique based on the so0-called velocity bunching (VB) scheme will make use of the first linac sections to provide longitudinal focusing [35]. We discuss in this section the design principles and the layout for both options.

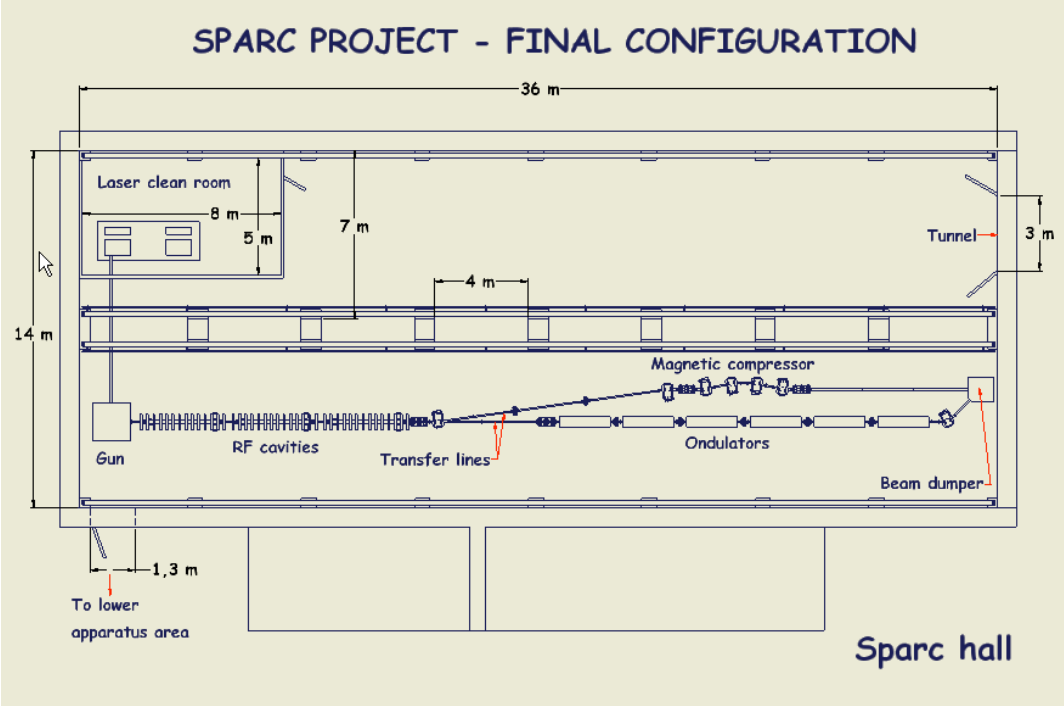

Figure 3.42 *– Schematic of SPARC – Phase 2*

3.9.1 Dog leg and bunch compressor line

The main transfer line connects the linac to the undulator on a straight line; a bending magnet after the first triplet deviates the beam into a line used for diagnostics, in particular for energy spread and slice emittance measurements. In Phase 2 it is foreseen to expand this section in order to have a parallel line for beam studies and a magnetic chicane for bunch compression experiments.

The first part of the line is a dogleg made of two bends and three quadrupoles which are used to cancel the dispersion function. A small bending angle (11°) has been chosen to minimize the perturbation on the beam; the distance between the parallel line and the main line is 1.67m, which allows access between the two lines. The distance between the first dogleg quadrupole and the main line is only 0.41 m; a layout drawing is needed to check for space availability.

A matching triplet is inserted between the dogleg and the magnetic compressor to adjust the minimum of the beta functions inside the compressor. The bunch compressor has a value of R_{56} = .141 m and of T_{566} = -.218 m. The dogleg contribution to R_{56} is negligible, R_{56} = -.003, but the contribution to T_{566} is large, T_{566} = -.48. The effects of second order terms on the bunch compression have been studied by simulations, and found to be insiginificant.

From PARMELA simulations the expected rms bunch length and relative energy spread are: σ_l = 1mm and σ_δ = 0.2%. The chosen value of R_{56} produces full compression of the bunch

for a correlated relative energy deviation □ lower than 1%. The displacement of the beam in the chicane is 0.30 m. In order to use the compressor between zero and the maximum, the design of a chamber with bellows and movable dipoles has to be studied.

The magnetic elements after the first dipole are described in Table 3.4, the first triplet is part of the main line. The beta and dispersion functions along the line are shown in Figs.3.43 and 3.44. The horizontal and vertical rms beam sizes are shown in Fig. 3.45 together with the beam envelope for an energy deviation □ = 1%. The initial conditions for the plots are: energy 150 MeV, rms normalized emittance 0.5 □m, $\beta_{x,y}$ 71 m and $\alpha_{x\,y}$ –4.

Table 3.4 - *Magnetic elements after the first dipole*

	Number	Length (m)	Angle	B (T) @150 MeV	G_{max} (T/m) @150 MeV
Dog leg dipoles	2	.26	11°	.37	
Compr. dipoles	4	.26	14°	.47	
Quadrupoles	9	.15			3.2

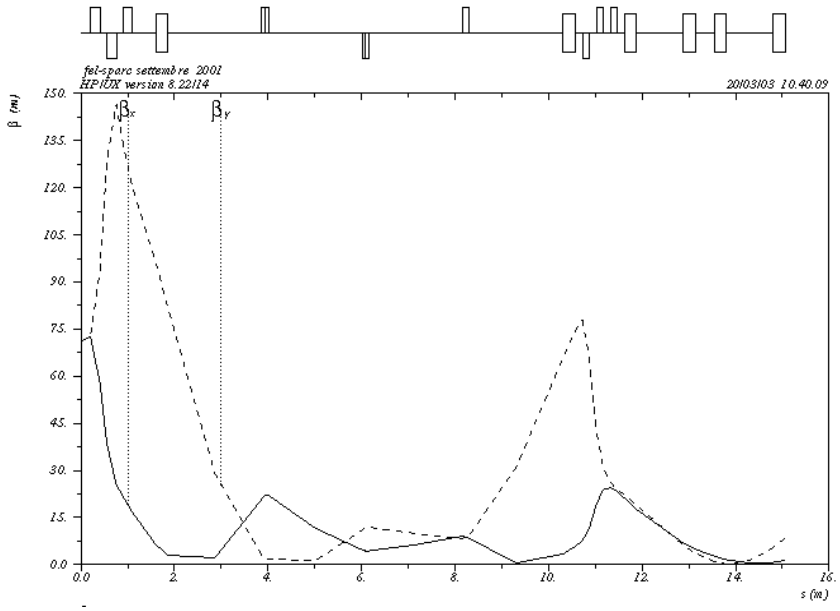

Fig. 3.43 *–Beta functions along the line*

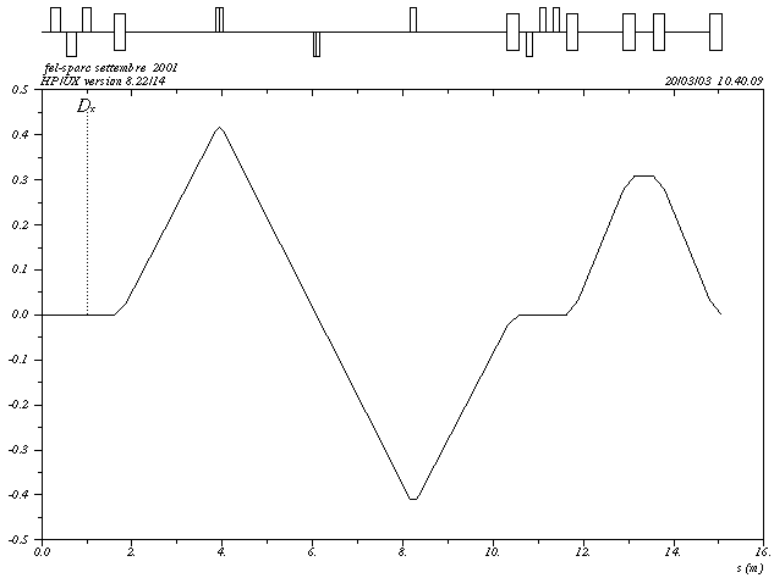

Fig. 3.44 *–Dispersion function along the dogleg line*

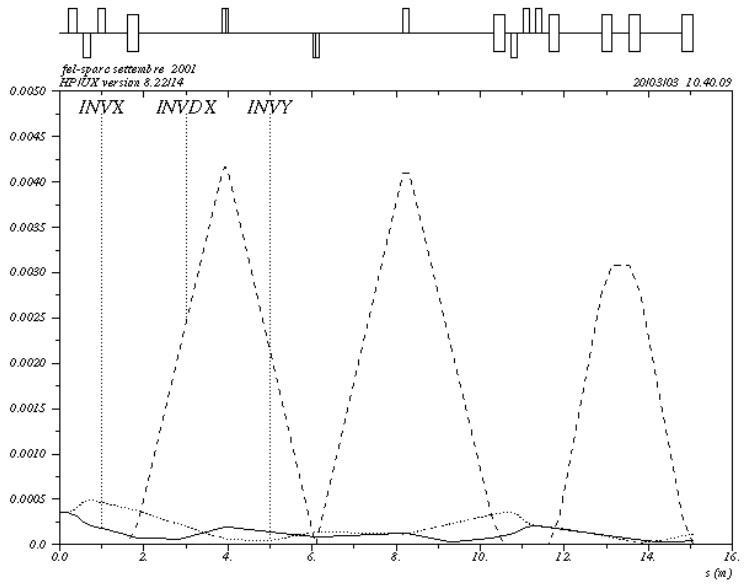

Figure 3.45 *–Beam envelope along the line: β_x (solid), β_y (dotted), D_x for δ = .01 (dashed).*

3.9.2 Velocity bunching design principles

The impact of magnetic compressors on the beam quality is quite relevant, with tendency to cause a serious emittance growth due to coherent synchrotron radiation [22] effects in their bends. The VB method, able to compress the bunch at moderate energies (tens of MeV) on rectilinear trajectories and integrated in the emittance compensation process, is in principle free from this source of emittance degradation. The theoretical model explaining velocity bunching is based on a Hamiltonian treatment as follows.

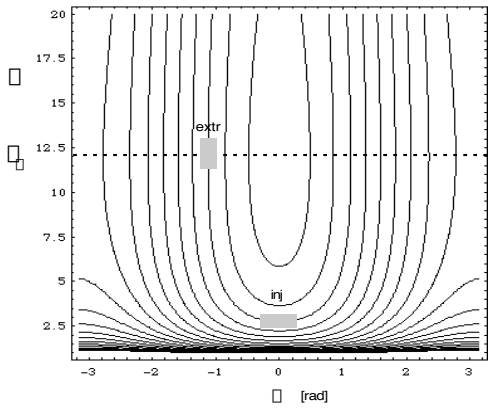

Figure 3.46 *–Phase space plots of a slow RF wave (γ_r finite) showing the basics of phase compression in a linac.*

The interaction of a beam with a RF wave given by $E_z = E_0 \sin(\omega t - kz + \varphi_0)$ is described by a Hamiltonian:

$$H = \gamma - \gamma_r \sqrt{\gamma^2 - 1} \cdot \cos\varphi \tag{3.20}$$

where γ is the normalized electron energy, $\varphi = kz - \omega t - \varphi_0$ is its phase with respect to the wave, while $a \equiv eE_0 / mc^2 k$ is the dimensionless vector potential amplitude and $\gamma_r = 1/\sqrt{1 - \beta_r^2}$ is the resonant gamma of the wave (conventional traveling wave structures operate at $\gamma_r = 1$, $k = \omega / \beta_r c$).

A wave whose phase velocity is slightly smaller than c, so that $k = \omega/c + \delta k$, is characterized by $\gamma_r = 1/c\delta k/\omega$, $\gamma_r = \sqrt{\omega/2c\delta k}$ (assuming $c\delta k/\omega << 1$).

The basic mechanism underlying the rectilinear compression effect is illustrated in Fig.3.46, where the contour lines of the Hamiltonian associated to a slow RF wave having γ_r= 12 (*i.e.* β_r = 0.9965 and β_k = 0.0035 ω/c) and a = 0.2 are plotted. If the bunch is injected into the wave at zero phase (*i.e.* when the field of the wave is not accelerating) at an energy lower than the synchronous one (which corresponds to φ_s), it will slips back in phase and go up in energy (being accelerated by the wave). By extracting the beam from the wave at the time it reaches the resonant φ_s, *i.e.* when it becomes synchronous with the wave, we make the bunch undergo one quarter of synchrotron oscillation. In doing that the beam is compressed in phase as depicted in the figure.

In order to preserve the beam transverse emittance we have to integrate the longitudinal dynamics of the RF compressor with the process of emittance compensation, which is achieved for a beam at constant current by matching it on the invariant envelope, as discussed in section 3.3. The analytical model is basically an extension of the invariant envelope theory [14], to the case of currents growing together with energy along the RF compressor [36]. The analysis reported in section 3.3 is valid only for beams carrying constant peak current I, as usual in photoinjectors when no compression mechanism is. In order to extend the model to the case of RF compression, where I grows by large factors, we have assumed that the current grows in the compressor at the same rate as the energy, i.e. $I = \frac{I_0 \gamma}{\gamma_0}$, where I_0 and γ_0 are the initial values for the current and the energy, respectively, at injection into the compressor. This assumption is derived by observations performed in several simulations of the RF compressor, indicating that best results in terms of final beam brightness are achieved under this condition of adiabaticity, which indeed gives rise to a new beam equilibrium.

The new exact analytical solution of the rms envelope equation becomes:

$$\beta_{RFC} = \frac{1}{\gamma\gamma'}\sqrt{\frac{I_0}{2I_A\beta_0}} \tag{3.21}$$

i.e. a beam flow at constant envelope (instead of $1/\sqrt{\gamma}$ as for the invariant envelope). This is dictated by a new equilibrium between the space charge defocusing term (decreasing now as $1/\gamma^2$) and the focusing and acceleration terms (imparting restoring forces to the beam): while for the invariant envelope equilibrium is achieved even in absence of external focusing , i.e. at $\gamma' = 0$, in this case we need to provide external focusing. A possible VB schememe is discussed in the next section.

3.9.3 Velocity bunching optimization for SPARC Test

The main purpose of the VB experiment at SPARC is to demonstrate the capability to increase the bunch peak current without degrading the emittance. As discussed in section 3 the emittance compensation process has to be tuned until the bunch goes from the laminar regime to the emittance dominated regime. SPARC phase 1 was in fact optimised for a 90 A beam up to 150 MeV. Operating the first TW structure in the VB mode and the other two TW structures in acceleration mode (on crest at maximum gradient 25+15 MV/m) will result anyway in a lower energy gain, about 120 MeV, still below the transition energy. For this reason we decided not to push the VB performance to its ultimate possibility (~ kA) [37] but to get experience of the emittance compensation process during bunching with a low compression ratio: 200 A at 120 MeV. Higher compression ratio will be also tested, even if the emittance compensation process won't be totally accomplished. In figure 3.47 are shown the possible VB working points versus the injection phase in the first TW structure.

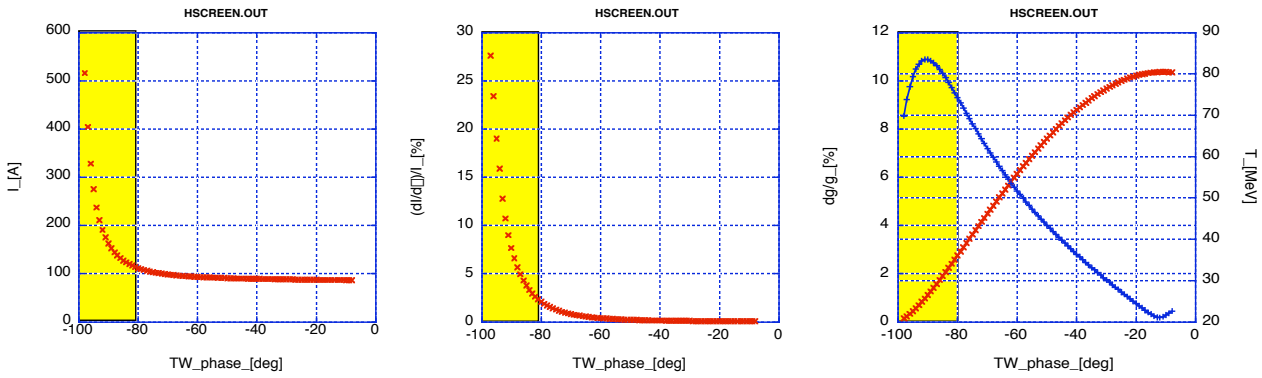

Fig. 3.47 *–Peak current (left plot), sensitivity to ± 0.5 deg phase jitter (central plot), rms energy spread (blue line, left plot) and energy gain (red line, left plot) versus injection phase in the first TW structure working at 25 MV/m accelerating field.*

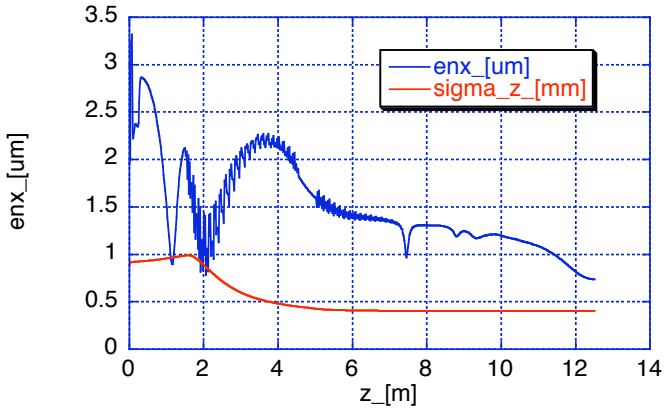

Fig. 3.48 *- rms normalised emittance and rms bunch length evolution along the beam line, injection phase –92 deg.*

Figure 3.48 shows the rms normalised emittance and rms bunch length evolution along the beam line for the –92 deg injection phase option. The bunching effect (a factor 2) of the first TW section, working at 25 MV/m, is clearly visible. The emittance compensation process requires now a more careful optimisation: during this experiment the three TW sections will be all embedded in solenoid fields (600-700 Gauss) to properly tune the beam plasma frequency as predicted by theory. At the exit of the third TW structure the emittance has reached a significant low value: 0.8 μm. The slice analysis reported in Fig. 3.49 shows that the slices carryng the higher peak current have also the best emittance. The rms energy spread results to be 1.8 % without any optimization.

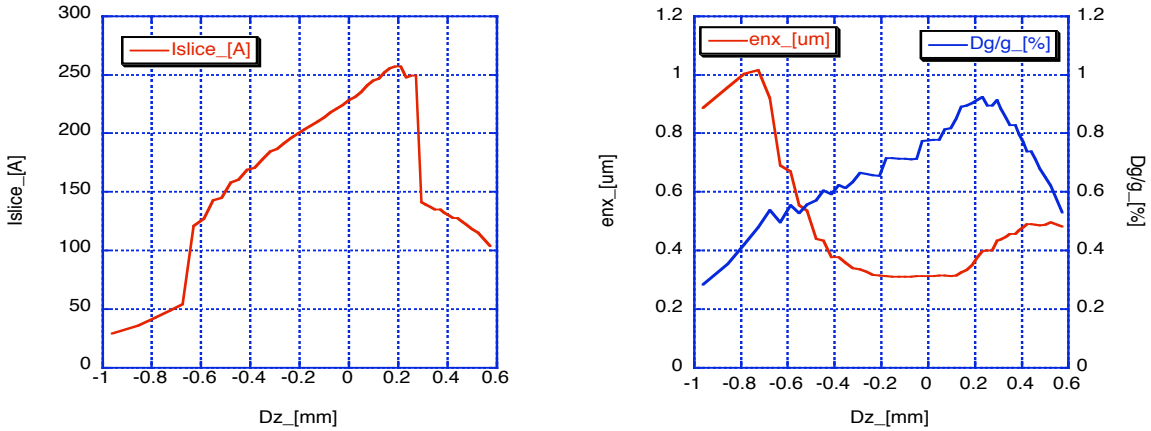

Fig. 3.49 *– Peak current (left plot), rms norm. emittance and rms energy spread (left plot) along the bunch at the exit of the linac, computed within 300 μm long slices.*

Sensitivity to phase jitters is one of the main investigation to do in order to integrate the VB technique in a larger scale FEL experiment, like the SPARX proposal. In the previous case simulations show that a phase jitter of ± 0.5 deg in the gun, would result in 10% fluctuation in the peak current at the exit of the linac. It has been shown that extending the bunching process over more than one TW structure working at a lower gradient is much better in terms of phase sensitivity [37]. In the next section a reduced gradient VB design is presented together with its possible integration in the SPARX design.

3.9.4 Integration of velocity bunching in SPARX: -jitters effects

An VB injector design more suitable to drive a larger scale FEL experiment and its integration in a 2 GeV linac [38], is discussed in this section. Higher brightness is achieved by increasing the compression ratio and with a more gentle emittance compensation by means of lower gradient TW structures embedded in stronger solenoid fields. In order to get a slow bunching of the beam and to increase the focusing magnetic field with the current during the compression process as prescribed by the theory, we used the first two sections as compressor stages. The RF compressor parameters set is shown in table xx. PARMELA calculations, done for a 1nC bunch 10 psec long (FWHM) with a rise time of 1 psec and 1 mm radius, show that with a proper setting of accelerating sections phase and solenoids strength it is possible to increase the peak current up to 300 A preserving the beam transverse emittance (Fig.3.50).

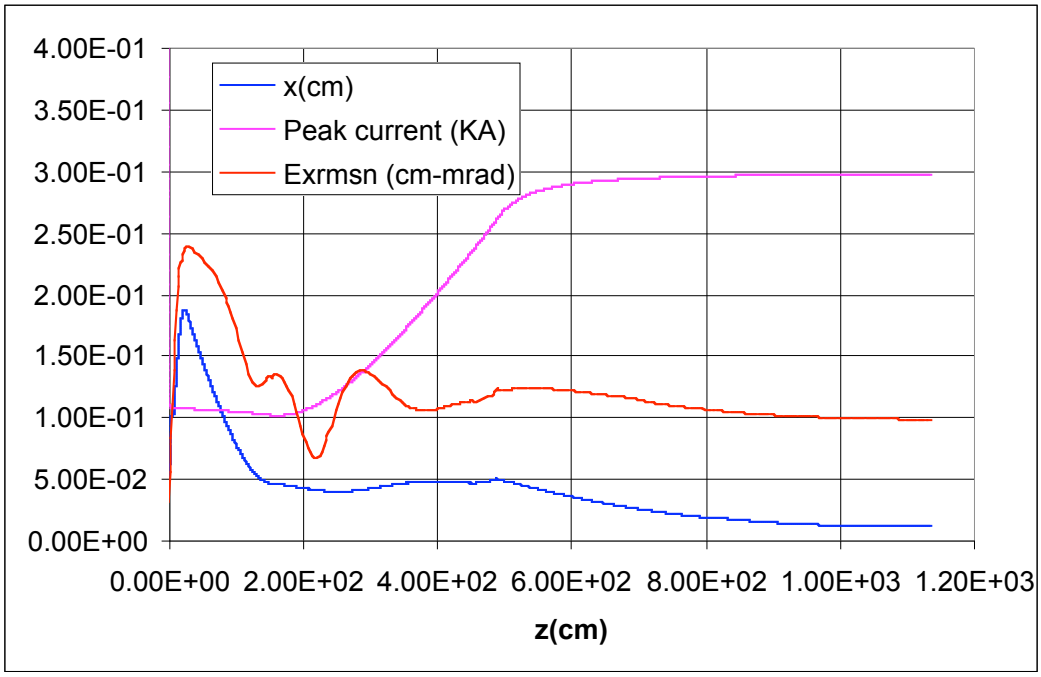

Fig. 3.50 *– Envelope, peak current, rms norm. emittance vs z*

The slices analysis (Fig. 3.51) of the output beam shows that the larger contribute to the projected emittance is given by the head and the tail of the pulse, while the emittance of the central part of the bunch is limited to 0.5 m. In addition it can observed that the bunch temporal distribution tends to a triangular shape: so the value of 300 A, that is simply scaled with the rms bunch length, is in reality an average current in the bunch corresponding to a larger value in the peak (about 500 A).

Table 3.5

TW section	***I***	***II***	***III***
Gradient (MV/m)	15	25	25
Phase (deg)	-86	-37	0
Solenoid field (G)	1120	1280	0

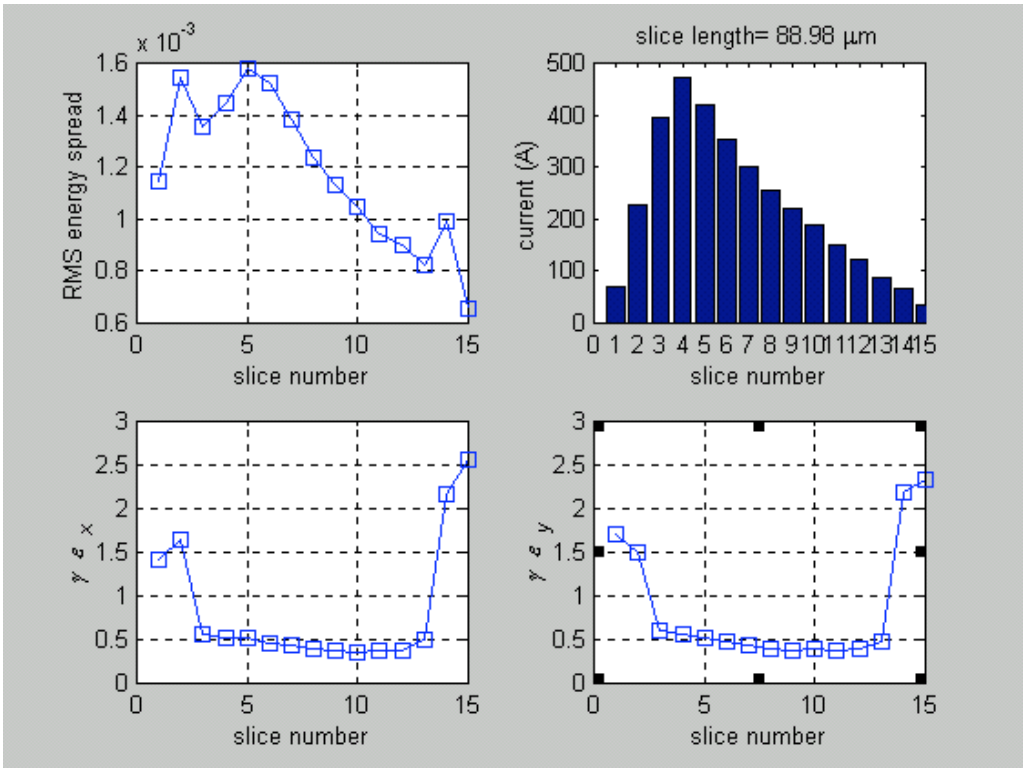

Fig. 3.51 *– Slice analysis of the SPARX beam after the compression*

A study of the sensitivity of peak current and emittance to phase jitter was done changing of ±1° the phase of the first TW structure. From the results shown in Table VIII it can be seen that changing the phase of ±1° produces a maximum variation of 13% in bunch length and 16% in normalized rms emittance.

Table 3.6

Phase on TW section I	**σ_z (μm)**	**Norm. rms emittance (μm)**
-87	251	1.16
-86	289	1
-85	324	0.87

One of the relevant aspects of the velocity bunching integration in the SPARX project is the phase jitter sensitivity of the combined VB and magnetic chicane compression system.

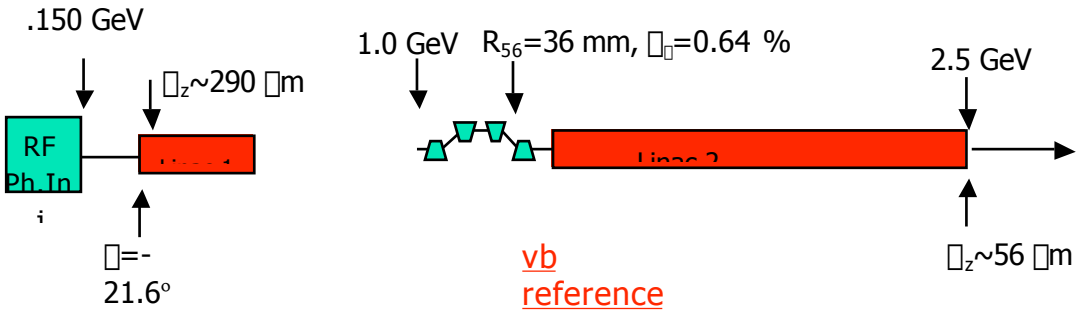

Fig. 3.52 *– Reference channel for the SPARX project.*

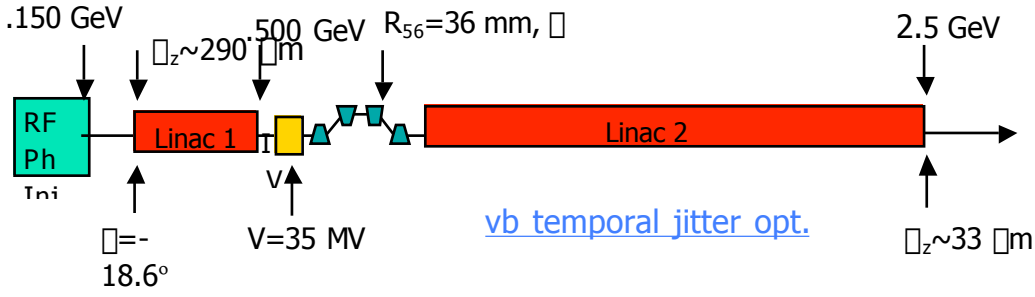

Fig. 3.53 *– Second layout with the temporal jitter optimization.*

The analysis has been performed dividing the channel in two parts: the RF compression stage and the rest of the channel that includes the high energy magnetic chicane. The first analysis has been devoted to the study and optimization of the channel downstream the RF compression system. Starting from the first channel layout, called "reference", shown in Fig. 3.52, an "optimized " channel has been developed that includes an X-band cavity to linearize the beam distribution before the second high energy magnetic compression stage, Fig. 3.53.

The goal was to find a setup of the channel that even with a timing error of 1 ps (1 deg) could reach the same final bunch length, Table 3.7 refers to the longitudinal analysis and optimization of the channel. With the help of the X-band cavity an increase in the bunch compression can be achieved without affecting the transverse emittance final value.

Tabe 3.7 *Optimization results for the velocity bunching SPARX channel.*

X_{band} Voltage (MV)	R56 (mm)	□ (°)	Energy@chicane (GeV)	□z (□m)	□z (□z=0.3 mm)	□□z (%)
35.0	37.28	18.6	0.51	30.5	30.6	0.5

The effect of a 1 ps temporal jitter, i.e. the laser pulse timing jitter, on the RF compressor has been analyzed first with the Parmela code, as discussed before, then the Parmela outputs have been tracked with Elegant on both the reference and the optimized channel and the results are reported in Tables 3.8 a) and b).

Table 3.8 a) *Summary table for the temporal jitter analysis on the optimized channel*

	σ_z(μm)	σ_δ(%)	ε_{nx}(μm)	$\Delta\sigma_z/\sigma_z$ (%)		
0	33.1	.15	3.0			
-1ps	31.8	.12	2.1	-3.9		
+1ps	36.0	.18	4.8	8.7		

Table 3.8 b): *Summary table for the temporal jitter analysis on the reference channel.*

	σ_z(μm)	σ_δ(%)	ε_{nx}(μm)	$\Delta\sigma_z/\sigma_z$ (%)		
0	56.0	.09	1.5			
-1ps	54.9	.11	1.0	2		
+1ps	57.9	.09	1.7	3.4		

These preliminary results show that the integration of a VB device in a higher energy linac with a second magnetic compressor stage do not cause additional concerns about the phase jitters. A more systematic analysis is under way in order to explore the full potentiality of such a hybrid scheme.

Appendix C: Extreme velocity bunching performances

It has been shown that the maximum compression achievable is mainly limited by the longitudinal emittance growth caused by RF curvature effects during the velocity bunching process. For the case of reference, the rms longitudinal emittance goes from 25 keV·mm at the exit of the RF gun up to 155 keV·mm at the exit of the RF compressor: the non-linear behavior of the accelerating field versus the accelerating phase introduces a curvature in the longitudinal phase space which is the source of longitudinal emittance.

As extensively discussed elsewhere [35], there are mainly two ways to increase the maximum compression achievable: one is the decrease in the accelerating gradient, the second is the use of higher harmonics to linearize the energy-phase correlation. The first method has the great disadvantage to require longer accelerating sections for the RF compressor, that should be operated at a lower gradient (below 10 MV/m).

The second method requires a dedicated RF structure operated at a higher harmonic: this option looks anyway more attractive, as discussed in the following.

The superposition of higher harmonics is indeed not conceivable inside the same slow wave structure of the compressor: it couldn't even be placed after the compression if this is pushed up to the overcompression limit, hence it's natural to conceive a lay-out in which the higher harmonic structure is placed before the compressor, i.e. in the drift between the gun and

the compressor itself. This drift (about 1 m long) is needed to accomplish the first part of the transverse emittance correction by properly focusing the beam plasma oscillations through it.

We therefore consider here a lay-out where a short (7 cell) third harmonic structure is placed right before the RF compressor. The RF compressor is operated with a slow wave corresponding to $\Box_r = 27$ ($\Box k = 0.07\%$), driven at 23 MV/m accelerating gradient, while the following structures are driven at 25 MV/m. The 3rd harmonic structure, being 8.2 cm long, is driven at 40 MV/m at a frequency of 8568 MHz (no detuning). Its role is indeed to pre-correct the RF induced curvature in the longitudinal phase space distribution as that shown: in order to achieve this task is actually enough that the total energy decrease induced by the 3rd harmonic structure is close to 1/9 of the total energy increase produced by acceleration into the RF compressor. This would in fact correct at least the second order derivative (scaling like n^2 , n being the harmonic number) of the phase space curvature, with a significant benefit to the longitudinal emittance. We actually found from simulations that best results are obtained for an energy decrease of about 3.5 MeV

The performances of the system are dramatically improved, thanks to the longitudinal emittance correction performed by the 3rd harmonic field, which brings it down to 25 keV·mm at the exit of the compressor, as opposed to 155 keV·mm without the 3rd harmonic correction. The beam current and energy throughout the Linac are plotted in Fig.C1.

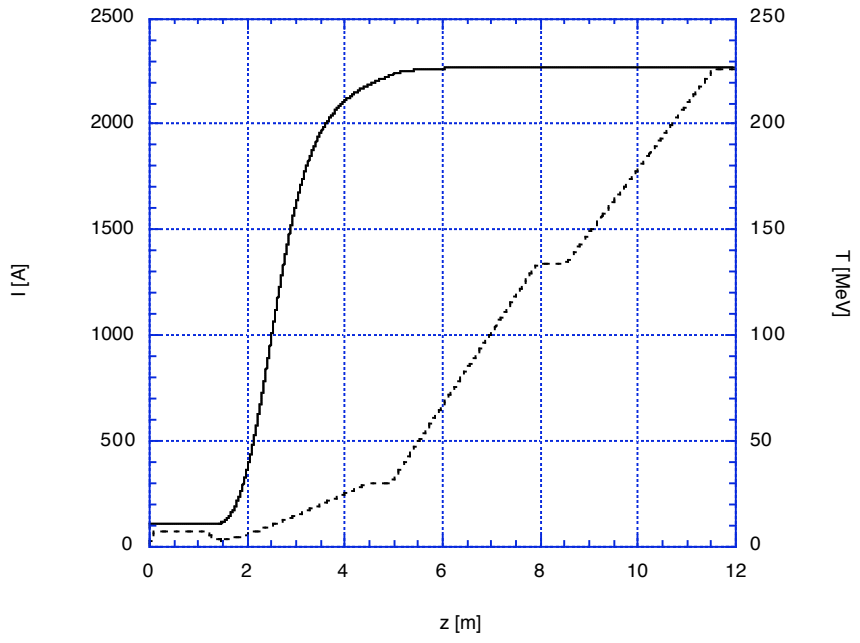

FIGURE C1. Beam current (solid line, left scale, in A) and energy evolution (dashed line, right scale, in MeV) through a 500 MeV Linac with implementation of a RF rectilinear compressor and a 3rd harmonic corrector.

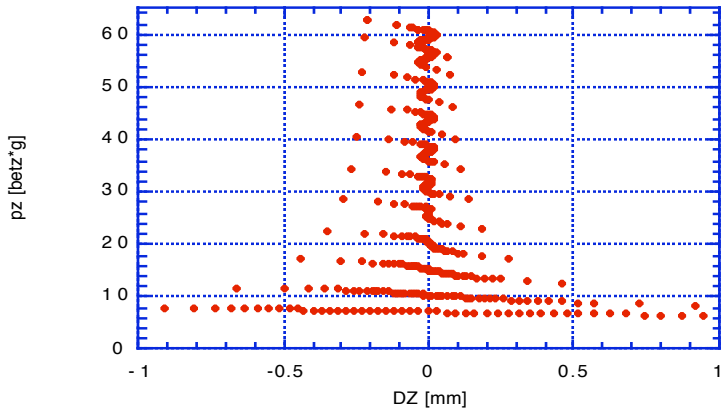

FIGURE C2. . Longitudinal phase space distributions taken at different times throughout the compressor for the case of total compression.

The final peak current value is 2.3 kA at full compression and a normalized rms transverse emittance below 1 mm·mrad, as predicted by Homdyn.

The compression is pushed in this case up to its maximum limit, as shown in Fig.C2, where the phase space distributions are plotted at various times throughout the compressor. The residual energy spread is totally uncorrelated to the phase, hence not recoverable any longer. This should be actually taken as an example of the potentials of this technique for producing ultra-short bunches: more extensive simulations with Parmela are certainly needed to validate these preliminary estimations and to find out the optimum operating point for the whole system.

The transverse dynamics is shown in Fig.14, where the rms beam envelope and normalized emittance are plotted along the Linac: the final emittance is still close to 0.55 mm·mrad, and this is again achieved by a careful setting of the field amplitudes and the locations of many solenoids placed around the RF compressor and the following two accelerating sections in order to keep focused the beam despite its increasing peak current. To this purpose, the RF compressor had to be placed closer to the RF gun exit, i.e. at 1.4 m far from the photocathode instead of 1.5 as for the LCLS nominal layout. Details of the transverse dynamics in this region are plotted in the lower diagram of Fig.C3.

A promising feature of this techinuqe is the production of fs bunches at low charge, of interest for injection into plasma accelerators: 30 fs bunches with 16 pC bunch charge have been predicted by simulations for a system based on RF compression quite similar to the SPARC photo-injector [37].

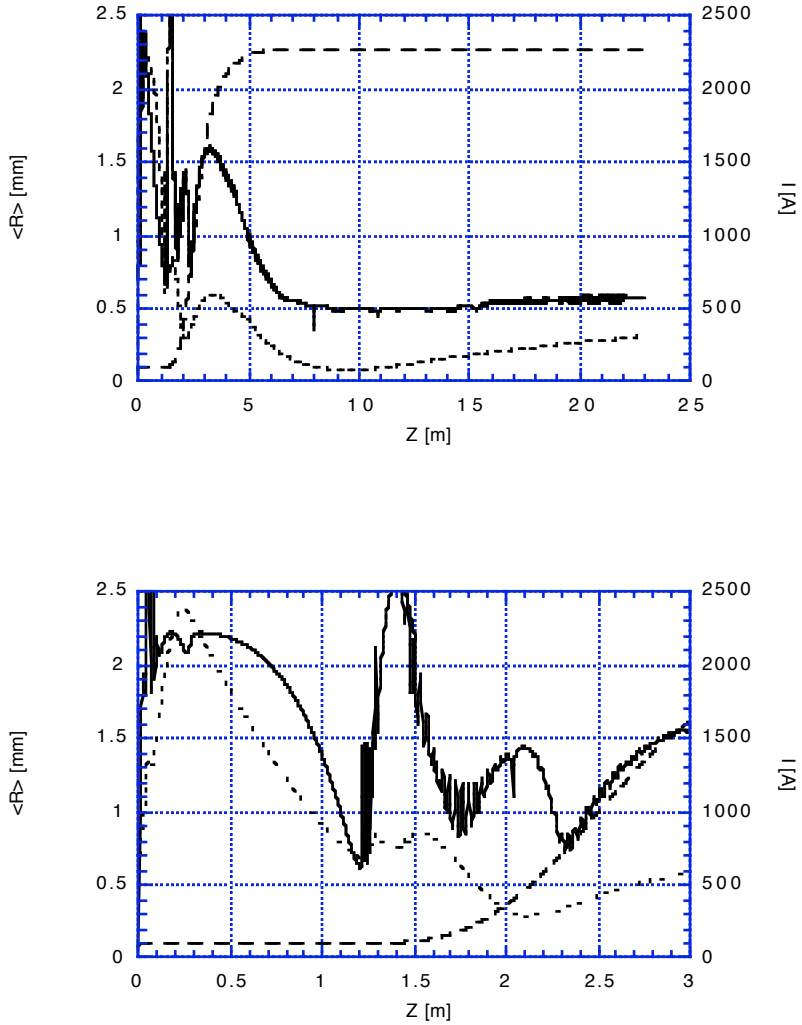

FIGURE C3. . Rms beam envelope in mm (dotted line, left scale) , rms normalized transverse emittance in mm·mrad (solid line, right scale) and beam peak current in A (solid line, right scale) along the Linac. The lower diagram shows the details of the upper one along the first 3 m of RF gun, drift, 3rd harmonic structure (from z=1.2 to z=1.28) and RF compressor (from z=1.4 to z=4.4)

ACKNOWLEDGMENTS

We like to thank R. Boni, A. Cianchi, A. Clozza, G. Dattoli, G. Di Pirro, A. Gallo, A. Ghigo, C. Sanelli, F. Tazzioli, C. Vicario, for the many detailed informations provided and all the people of the laser, RF and diagnostic groups for the many helpful discussions and suggestions.

REFERENCES

[1] M. Borland et al., “Start to end simulation of SASE FEL from gun through the undulator”, Nucl. Instr. & Meth. A 483 (2002) 268-272.
[2] J. Billen, “PARMELA”, LA-lUR-96-1835, 1996.
[3] E.Colby, “Design, Construction and Testing of a Radiofrequency Electron Photoinjector for the Next Generation Linear Collider, PhD Thesis, UCLA 1997.
[4] M. Ferrario et al. “Multi bunch energy spread induced by beam loading in a standing wave structure”, Particle Accelerators 52, 1 (1996)
[5] L. Giannessi, M. Quattromini, Submitted to PRST AB (2003).
[6] Y. H. Chin, “Advances and applications of ABCI”, Proc of PAC 93, Washington D.C. 1993.
[7] M. Borland, “elegant: A Flexible SDDS-Compliant Code for Accelerator Simulation” LS-287, ANL, Argonne, IL 60439, USA.
[8] CERN Report CERN/SL/90-13 (AP) (1995)
[9] S. Reiche, Nucl. Instrum. & Meth. A429,243 (1999).
[10] R. A. Jong, W. M. Fawley, and E. T. Scharlemann, “Modelling of induction-linac based free-electron laser amplifiers,” in Modeling and Simulation of Laser Systems, Proc. SPIE 1045, pp. 18–27, 1989.
[11] S.G. Biedron, H.P. Freund, S.V. Milton, “3D FEL code for the simulation of a high-gain harmonic generation experiment, in: Harold E. Bennett, David H. Dowell (Eds.), Free-Electron Laser Challenges II, Proc. SPIE 3614, (1999).
[12] L. Giannessi, http://www.perseo.enea.it
[13] ENEA Report RT/INN/93/09 (1993).
[14] L. Serafini, J. B. Rosenzweig, "Envelope analysis of intense relativistic quasilaminar beams in rf photoinjectors: a theory of emittance compensation", Phys. Rev. E **55** (1997) 7565.
[15] J. Clendenin et al., “Reduction of thermal emittance of rf guns”, SLAC-PUB-8284 (1999)
[16] S. G. Anderson and J. B. Rosenzweig, “Non-equilibrium transverse motion and emittance growth in ultrarelativistic space-charge dominated beams”, Phys. Rev. ST Accel. Beams 3, 094201 (2000).
[17] M. Ferrario et al., “HOMDYN Study For The LCLS RF Photo-Injector” Proc. of the 2nd ICFA Adv. Acc. Workshop on “The Physics of High Brightness Beams”, UCLA, Nov., 1999, see also SLAC-PUB-8400.
[18] Linac Coherent Light Source (LCLS) Conceptual Design Report, SLAC-R-593 (2002).
[19] M. Ferrario, K. Flöttmann, B. Grigoryan, T. Limberg, Ph. Piot, “Conceptual Design of the TESLA XFEL Photoinjector”, TESLA-FEL 2001-3.
[20] ORION Technical Design Study, ORION006.
[21] M. Ferrario et al., “Recent Advances And Novel Ideas For High Brightness Electron Beam Production Based On Photo-Injectors”,to be published in The Physics & Applications of High Brightness Electron Beams, J.Rosenzweig and L.Serafini ed., World Sci.
[22] P. Emma, “Accelerator physics challenges of X-rays FEL SASE sources”, Proc. Of EPAC-02, Paris 2002.
[23] M. Xie, “ Design optimization for an X-ray Free Electron Laser driven by SLAC linac”, Proc. of PAC-95, Dallas 1995.
[24] C. Limborg, “New optimization for the LCLS photo-injector”, Proc. Of EPAC-02, Paris 2002.
[25] F. Zhou, I. Ben-Zvi, M. Babzien, X. Y. Chang, A. Doyuran, R. Malone, X. J. Wang, and V. Yakimenko , “Experimental characterization of emittance growth induced by the nonuniform transverse laser distribution in a photoinjector”, Phys. Rev. ST Accel. Beams 5, 094203 (2002).

[26] J. Yang et al., “Low-emittance electron-beam generation with laser pulse shaping in photocathode radio-frequency gun”, J. of App. Phys. V 92, N. 3, 1608, August 2002.
[27] R. Carr et al., “Visible-infrared self-amplified spontaneous emission amplifier free electron laser undulator”, Phys. Rev. ST Accel. Beams 4, 122402 (2001).
[28] S. Anderson, J.B. Rosenweig et al. “ Space-charge effects in high brightness electron beam emittance measurements”, Phys. Rev. Special Topics – Acc. and beams, Volume 5, 014201 (2001).
[29] M. Zhang “Emittance Formula for Slits and Pepper-pot measurement”, FERMILAB-TM-1998
[30] D.H. Dowell “Bellows-Induced Wakes in the Pepper Pot Experiment”, private communication.
[31] K.Bane M. Sands, “Wake Fields of Very Short Bunches in an Accelerating Cavity”,SLAC-Pub-4441
[32] D.H. Dowell *et al*, “Slice Emittance Measurements at the SLAC Gun Test Facility”, SLAC-PUB-9540, September 2002
[33] J.F. Schmerge *et al*, “Transverse-emittance measurements on a S-band photocathode RF electron gun”, Nucl. Instr. & Meth. A 483, 2002, pp. 301-304
[34] X. Qiu *et al* ,”Demonstration of Emittance Compensation through the Measurement of the Slice Emittance of a 10- ps Electron bunch”, Phys. Rev. Lett. 76, 20, 1996, pp. 3723-3726.
[35] L. Serafini, M. Ferrario, “Velocity Bunching in PhotoInjectors” , AIP CP 581, 2001, pag.87.
[36] M. Boscolo et al., "Beam Dynamics Study of an RF Bunch Compressor for High Brightness Beam Injectors", Proc. of EPAC2002, Paris.
[37] L. Serafini, M. Ferrario, A. Bacci, “Ultra-Short Electron Bunch Generation with Rectilinear Compressor” Proc. Of PAC 01, Chicago 2001.
[38] D. Alesini et al., “Conceptual Design of a High-Brightness Linac for Soft X-ray SASE-FEL Source”, Proc. Of FEL Conf., Chicago 2002.
[39] J. B. Rosenzweig and E. Colby, Charge and Wavelength Scaling of RF photoinjector design, TESLA-95-04.